Measurements of the Spin Rotation Parameter Q as a Test of Pauli Blocking in Proton-Nucleus Elastic Scattering

by

Ma Ji

B.Sc. The University of Science and Technology of China

People's Republic of China, 1982

THESIS SUBMITTED IN PARTIAL FULFILLMENT OF

THE REQUIREMENT FOR THE DEGREE OF

MASTER OF SCIENCE

in the Department

of

Physics

SIMON FRASER UNIVERSITY

July 1987

APPROVAL

Name: Ma Ji

Degree: Master of Science

Title of thesis: Measurements of the Spin Rotation Parameter Q as a Test of Pauli Blocking in Proton-Nucleus Elastic Scattering

Examining Committee:

Chairman: Dr. D. H. Boal

Prof. Otto Häusser
Senior Supervisor

Prof. K. S. Viswanathan

Dr. K. P. Jackson
Examiner
Research Scientist, TRIUMF

Date Approved: August 10, 1987

PARTIAL COPYRIGHT LICENSE

I hereby grant to Simon Fraser University the right to lend my thesis, project or extended essay (the title of which is shown below) to users of the Simon Fraser University Library, and to make partial or single copies only for such users or in response to a request from the library of any other university, or other educational institution, on its own behalf or for one of its users. I further agree that permission for multiple copying of this work for scholarly purposes may be granted by me or the Dean of Graduate Studies. It is understood that copying or publication of this work for financial gain shall not be allowed without my written permission.

Title of Thesis/Project/Extended Essay

Measurements of the Spin Rotation Parameter Q as a Test of Pauli Blocking in Proton-Nucleus Elastic Scattering

Author:

(signature)

Ma Ji

(name)

Aug. 19, 87

(date)

ABSTRACT

The spin rotation parameter (Q) and vector analyzing power (A_y) have been measured for $\vec{p}+{}^{208}Pb$ and $\vec{p}+{}^{90}Zr$ elastic scattering at 200 MeV using the medium resolution spectrometer and focal plane polarimeter at TRIUMF. These results together with differential cross section data from a previous TRIUMF experiment uniquely determine the elastic scattering matrix up to an overall phase. The spin rotation parameter Q is more sensitive than A_y and σ to the differences between N-nucleus reaction models. A parameter-free relativistic impulse approximation calculation shows that inclusion of Pauli blocking modifies strongly the spin observables, especially Q, in nucleon-nucleus reactions. Our results at 200 MeV strongly support the relativistic calculation which invokes Pauli blocking. In addition we have calculated a non-relativistic microscopic optical potential using a nuclear matter approach. The only input is the Paris potential and ground state densities for both protons and neutrons. We find that the experimental data are not as well reproduced as in the relativistic approach.

DEDICATION

To my father and mother.

ACKNOWLEDGEMENTS

First, I would like to thank my supervisor Prof. O. Häusser and Dr. M. Vetterli for proposing and planning this experiment and for their critical comments. I also benefitted from discussing with them details of the experiment. I also like to thank Dr. K. Hicks for many comments and discussions on the off-line analysis of the data. I am grateful to all collaborators of this experiment who made contributions to the success of this experiment. Discussions on physics concepts with Dr. R. Jeppesen, who provided many of his programs and their descriptions are specially acknowledged.

Contents

List of Figures

Chapter 1

Introduction

Studies of elastic proton scattering from nuclei at intermediate energies have received much attention during the last decade. There are two motivations. First, one would like to quantitatively describe the proton-nucleus scattering observables in terms of nucleon-nucleon phenomenology. Second, after having obtained a successful working model of the proton-nucleus interaction, one would then proceed to infer new nuclear structure information from inelastic scattering data.

At an early stage, N-nucleus scattering phenomena were handled mainly by means of the standard phenomenological optical model involving Woods-Saxon form factors for the complex central potential. It has the familiar form:

$$U_c = V_o f_R(r) + iW_o f_I(r)$$

with the Woods-Saxon function,

$$f_x = \frac{1}{1 + exp^{\frac{(r-R_x)}{a_x}}} \qquad (x = R, I)$$

The standard spin-orbit potential is also a complex potential of the conventional Thomas form which involves the derivative of a Woods-Saxon function

$$U_{so} = [V_{so} g_R(r) + iW_{so} g_I(r)] \vec{L} \cdot \vec{\sigma}$$

where

$$g(r) = \frac{1}{r}\frac{d}{dr}f(r),$$

σ are the Pauli matrices and L are orbital angular momenta of nucleons inside the nucleus. In the conventional optical calculation, these potentials are inserted into the Schrödinger equation which at these energies incorporate some minimal relativity, i.e. involves at least relativistic kinematics and, in addition, frequently involves a replacement of the reduced mass by a reduced total energy.

Then comes the second stage, the proton-nucleus interaction is described from first principles–the microscopic model, with a microscopic description of the effective interaction between the projectile nucleon and the target nucleus. Theoretical progress on this topic has mainly taken place from 1968 to 1978 [1]. One assumes that the NN interaction may be adequately described by a two body potential. All models can be divided into two groups, relativistic and nonrelativistic ones. The nucleon-nucleon free scattering amplitudes are the most important input quantity needed in proton nucleus optical potential calculations.

Many different approaches successfully describe experimental data at 500 MeV and above (for example, relativistic impulse approximation [2] (RIA) and KMT multiple scattering theory [35] and non-relativistic impulse approximation (NRIA) etc). As the bombarding energy decreases, the discrepancies between theory and data became more and more severe. Both these models were explored in an attempt to solve these large discrepancies. All these attempts were found to be incapable of explaining the data. It was concluded that medium effects (i.e. Pauli blocking and binding correction effects in intermediate states) must be responsible for these difficulties. The first working model to include these medium modifications was the Von Geramb model [3]. The effective t-matrix in this model depends on the density of the medium, thus the potential is

also density dependent. This density dependent effective interaction has been applied to proton nucleus scattering by constructing the optical potential through the local density folding model [3].

$$U(\vec{r}) = \int d^3r'\, t\,(|\vec{r} - \vec{r}'|, \rho(\vec{r}))\, \rho(\vec{r}')$$

This model is more successful than the NRIA and has been used for comparison with the present results.

The interest in the relativistic aspects of the nuclear structure has increased in the past few years. The relativistic approach started with the Lorentz invariant scattering amplitude of the NN interaction and the Dirac equation with the simplest assumption that the medium corrections for the effective interaction are unimportant(impulse approximation,RIA). The effective interaction was represented by a Love-Franey type parameterization of the free two-nucleon t-matrix. This model was highly successful in explaining data at energies near E=500 MeV or above and failed to reproduce data at lower energy [4].

At the AIP conference in 1982, P. Schwandt reviewed all available experimental data for nucleon-nucleus elastic scattering in the intermediate energy regime [1]. He pointed out that relativistic and standard optical models, although they fit the differential cross section (σ) and polarization (P) quite well , both fail to reproduce spin rotation parameter (Q) data. This suggests that measurements of, Q in addition to σ and P data, are essential to determine the realistic optical model potentials. Thus complete measurements of spin observables (σ, P, Q) in $(\vec{p}, \vec{p})$ elastic scattering have played a major role in the development of the optical models of the nucleon-nucleus interaction at intermediate energy region. After that, many experiments have been done to measure spin rotation functions[4][5][6]. Experimental progress has greatly pushed forward the

studies of optical model potential.

Recently Horowitz [7] and others solved some difficulties of the relativistic impulse approximation (RIA) at low energy by the use of pseudovector coupling instead of pseudoscalar πN coupling, and the exact treatment of the exchange terms. Pauli blocking was used in modifying the final optical potential. Calculations then correctly reproduced the available cross sections and spin observables. This was not the case in the nonrelativistic approach at that time. However the importance of medium effects due to Pauli blocking remained an open problem in the RIA. Horowitz and Murdock [7] predicted large Pauli blocking effects, while Wallace obtained good description of $^{40}Ca(\vec{p},\vec{p})$ at 181 MeV data without involving such an effect[8]. Our choice of energy was motivated by the available data from IUCF on ^{12}C, ^{16}O, ^{40}Ca, and ^{48}Ca at this energy [8]. Our measurement fills the high-A end in this data set to provide a systematic study of the dependence of the interaction as a function of target mass. Our ^{208}Pb data , together with the 290 MeV TRIUMF data [4] where Pauli blocking already shows large effects on the spin rotation function, and the 500 MeV and 800 MeV data from LAMPF [5], will complete a study of the energy dependence of the N-nucleon interaction.

This experiment was primarily designed to test Pauli blocking effects in the relativistic microscopic optical model. The installation of the focal plane polarimeter (FPP) enables the medium resolution spectrometer (MRS) to measure the transverse polarization components of scattered protons. These components are necessary to calculate the Wolfenstein spin transfer parameters and eventually obtain the spin rotation function Q. We measured the spin rotation function for both ^{208}Pb and ^{90}Zr at a projectile energy of 200 MeV. These data together with TRIUMF cross section data at the same energy [9], completely determine the scattering matrix up to a phase. The scattering angles ranged from 3° to 40°, where the Pauli blocking effects are expected to be pronounced.

In the experiment, the target thickness and the running time increased with angle to compensate for the decreasing cross section. After we finished data analysis, we performed the nonrelativistic microscopic model calculation using the density dependent Hamburg-Paris NN potential [10] to generate the optical potential. Spin observables were calculated using ECIS87 [11]. We should stress here that the only other input to our calculations are the proton and neutron density parameters which were taken from electron scattering data [12][13], no fitting was done in our calculation. The calculations reproduce all the observables quite well. The relativistic calculation has been done by Horowitz and Murdock [7]. Except where it misses one small structure in the spin rotation function, this theory reproduces our data equally well. Since spin observables are sensitive to off-shell scattering amplitudes, our measurement also gives some constraint on the form of off-shell scattering amplitudes which is very important when choosing the πN coupling.

We provide a brief introduction to the conventional microscopic nonrelativistic and relativistic models in Chapter Two. Chapter Three is dedicated to the description of the experimental enviroment and the apparatus. The derivation of spin observables and the data analysis is presented in Chapter Four. Finally results and conclusions are offered in Chapter Five.

Chapter 2

Theoretical Background

Since we are dealing with the many-body system in terms of elementary two body forces, an accurate theoretical calculation is not feasible. Such theoretical problems are usually solved by models with reasonable assumptions about nuclear structure. The theoretical results are then compared with experimental data, to judge which model most closely describes the real nucleus. There are two types of theories which both successfully reproduce physical observables at intermediate energies. They are both microscopic models based on the fundmental NN interaction. The relativistic approach stresses the importance of relativistic effects, assumes very small medium modifications and treats target nucleons as quasifree thus allowing the impulse approximation to be used. The results of the effective NN interaction (Lorentz covariant represenetation of the NN amplitude [7]) is folded with the density of the nucleus calculated from a relativistic Hartree method [14] to generate the optical potential. This potential is used in solving the Dirac equation to obtain the scattering wavefunction. Finally physical observables are calculated by taking expectation values of the proper operators. The nonrelativistic theory starts with a calculated fundamental NN interaction matrix(Paris t-matrix) [10]. Pauli blocking was included by solving the Bethe-Goldstone integral equation instead

of the Lippmann-Schwinger equation, which does not contain the Pauli projection operator. To take the Fermi motion into account, we need to average the free scattering amplitude for all target nucleons with different Fermi momentum. Finally binding energy corrections are taken into account. Again, in the same way that was employed in the relativistic calculation, by solving the Schrödinger equation one can obtain the scattered waves. Thus these models give theoretical predictions for physical observables. Relativistic kinematics are used in the nonrelativistic calculation. Differences in the predictions thus purely reflect differences in the interaction mechanism. Spin observables are especially sensitive to the different flavors of the models and serve as efficient tests of the models. In the first part of this chapter we briefly review the nonrelativistic microscopic optical model. In the next section, the relativistic microscopic model is presented and finally the differences between these two models are described.

2.1 Nonrelativistic Microscopic Nuclear Matter Approach

We wish to define a potential which, when inserted into the Schrödinger equation gives, in an energy range sufficiently below the meson production theshold, the correct description of elastic scattering. The nucleon-nucleus optical potential is obtained by folding the matter density of the finite nucleus with the complex nucleon-nucleon effective interaction, t-matrix, which describes the effective interaction between the incident nucleon and a particular nucleon in the target nucleus. The t-matrix is calculated from a given realistic NN potential (Paris NN potential) using a Bethe-Goldstone type integral equation (which means it includes a Pauli blocking medium modification) [3]. It determines the two-body transition operator in applications to finite nuclei using a local density ap-

proximation. This approach is commonly referred to as the nuclear matter microscopic model. It has been established as a quantitative method to describe nucleon-nuleus scattering and constitutes a fundamental step in understanding the nuclear many body problem.

2.1.1 The Paris NN potential

The Paris potential is a NN interaction derived from πN and $\pi\pi$ interactions [17], which includes the one pion exchange(OPE), correlated and uncorrelated two pion exchange, and ω exchange contributions. These theorical contributions give a fairly realistic description of long and medium range (LR+MR) NN forces. Since the short range(SR) part of interaction is related to exchange of heavier mesons or to effects of subhadronic constituents such as quarks and gluons, there is no theoretical reason to believe the validity of this potential below the range of internucleon distances ($r \leq 0.8fm$). No reliable calculations of this SR part are available. Thus the SR part should be determined phenomenologically, with the hope that the accurately determined LR+MR interaction will provide strong constraints on this SR part, leaving us only a few degrees of freedom. It was proposed to describe the core with a very simple phenomenological model; namely, the long and intermediate range ($\pi + 2\pi + \omega$) potential is cut off rather sharply at internucleon distances ($r \sim 0.8fm$) and the short range ($r \leq 0.8fm$) is described simply by a constant soft core and a linear extension of the LR+MR part to the SR part. Experimental data support this assumption. The slope of the energy dependence is determined by fitting all the known phase shifts($J \leq 6$) up to 330 MeV and parameters of the deuteron.

The Paris NN potential was purposely chosen in this simplest form to demonstrate that, once the LR+MR forces are accurately determined, the SR force can be described

by a model with few parameters that does not affect the LR+SR part. This simple model in which a definite separation between the theoretical and phenomenological part is made, is designed to provide a clear physical insight into the problem.

2.1.2 General Principles

The optical potential is obtained by the usual Hartree-Fock method [14]. A nucleon with energy E and momentum k moving in an infinite system with Fermi momentum k_F feels an average complex potential $U(k_F, k, E) = -V - iW$ whose leading term is given by [3]

$$U(k_F; k, E) = \sum_{p<k_F} < pk|t(\omega)|pk >_A$$

In this equation $\omega = E + e(p)$, where $e(p)$ is the single-particle energy of a bound nucleon of momentum p and $< pk|t(\omega)|pk >_A$ are the two body antisymmetrized matrix elements of the transition operator $t(\omega)$ defined by the integral equation

$$t(\omega) = V - VG(\omega)t(\omega)$$

where V is the nucleon-nucleon effective interaction calculated from the Paris potential and $G(\omega)$ is the Green's function (propagator) for the nucleon pair:

$$G(\omega) = \frac{Q_P(q_1, q_2)}{e(q_1) + e(q_2) - \omega + i\varepsilon}$$

where q_1 and q_2 are the momenta of nucleons in the intermediate states and $Q_P(q_1, q_2)$ is the Pauli projection operator

$$Q_P(q_1, q_2)|q_1, q_2 >= \begin{cases} |q_1, q_2 > & \text{if } q_1, q_2 > k_F \\ 0 & \text{otherwise.} \end{cases}$$

This operator is used to include Pauli blocking. The eigenvalue equations indicate that only the intermediate states which are above the Fermi sea could contribute, in accordance with the Pauli principle.

The single particle energy $e(q)$ should be taken self-consistently:

$$e(q) = \frac{q^2}{2m} + U(k_F; k, E)$$

The t-matrix in the nuclear matter approach is local in coordinate space and depends on the energy E and density ρ_{NM} and has many pieces:

$$t(r, \rho_{NM}, E) = t_c(r, \rho_{NM}, E) + t_{s.o.}(r, \rho_{NM}, E)\vec{L} \cdot \vec{S} + \text{other terms.}$$

Other terms refers to other components of the t-matrix (for example tensor) which are not important for a scattering from a spin zero nucleus at intermediate energies. Each t-matrix component creates the corresponding piece of the optical potential. Since spin observables are especially sensitive to the spin-orbit part of the interaction, we pay more attention to it. Detailed calculations show that [18]

$$U_{s.o.}(r, E) = \frac{1}{3}\pi[F_{pp}(r, \rho, E)\frac{1}{r}\frac{\partial \rho_p}{\partial r} + F_{pn}(r, \rho, E)\frac{1}{r}\frac{\partial \rho_n}{\partial r}]$$

where $\rho = \rho_p + \rho_n$, $\rho_{p(n)}$ is the proton (neutron) density and the coeffients F_{pp} and F_{pn} depend on the spin-orbit t-matrix elements and the local densities. The $\frac{1}{r}\frac{\partial \rho}{\partial r}$ dependence gives a peak located at the nucleus surface (See Fig. 2.1). Polarization has been shown to be sensitive to the spin orbit potential used. As we reduce the spin-orbit potential by a factor of two, the calculated value obviously underestimates the data at small angles.

This optical potential should be localized to take into account the finite size and geometry of the nucleus. The simplest prescription for calculating the radial dependence of the optical potential is the local density approxmation. The idea of this approxmation is to assume that at each point inside the nucleus the value of the optical potential U can be calculated from the value of the density at that point in nuclear matter.

Three-parameter Gaussian distributions were chosen for neutron and proton densities:

$$\rho(r) = \rho_o(1 + \frac{\omega r^2}{c^2})/(1 + exp(\frac{r^2 - c^2}{z^2}))$$

Parameters were taken from electron scattering and proton scattering data (See table 2.1)

nucleus	set	ω	c[fm]	z[fm]	ref.
^{208}Pb	ρ_p	0.3379	6.3032	2.8882	[12]
	ρ_n	0.36	6.19	3.13	[13]
^{90}Zr	ρ_p	0.245	4.522	2.5216	[12]
	ρ_n	0.56	4.49	2.45	[13]

Table 2.1: Nuclear radius parameters for 3-parameter Gaussian distributions

We used the computer code MAINX8 which follows the non-relativistic microscopic nuclear matter approach to generate the optical potential. This calculation contains all three kinds of medium modifications (Fermi motion, binding energy correction and Pauli blocking). It was found that this potential, when fed into ECIS87 [11], could not reproduce the cross sections published in ref. [3]. It turns out that when we use relativistic kinematics for non-relativistic calculations, the Schrödinger equation should use the reduced mass rather than the reduced total energy as was used in the non-relativistic calculation with non-relativistic kinematics. The ratio of reduced mass to reduced total energy is 0.827 for ^{208}Pb and 0.830 for ^{90}Zr . Once we included this factor in the optical potential, the calculations reproduce the cross section and spin observables. Fig. 2.1 shows the separate parts of the optical potential. It should be noted that the correction factor (i.e. ratio of reduced energy to the reduced mass) has frequently been omitted in the literature. In spite of successfully reproducing the spin observables, the ambiguities about this factor still exist. A justification of this factor will be given in the last chapter.

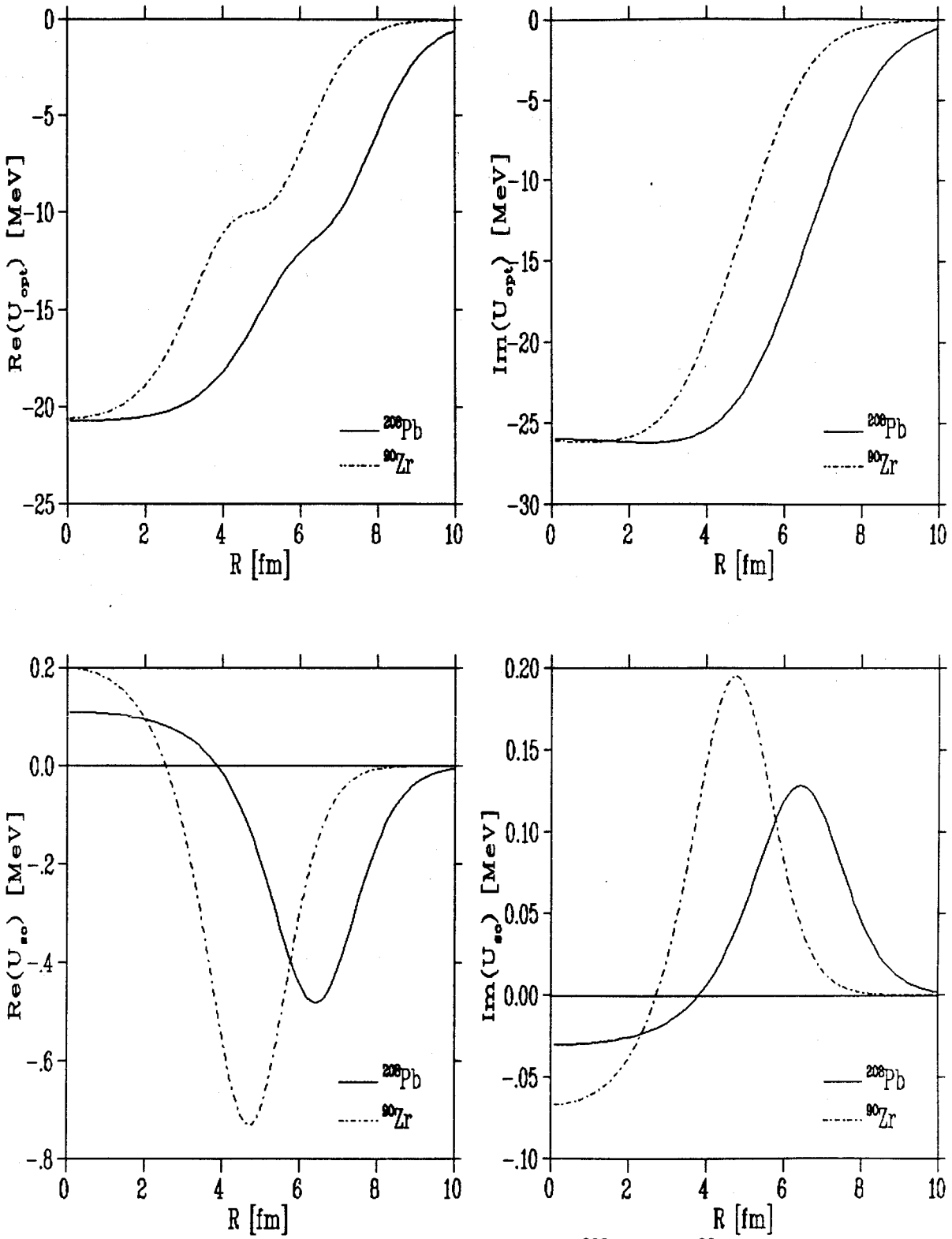

Figure 2.1: Microscopic optical model potential for ^{208}Pb and ^{90}Zr at 200 MeV. Top two plots are central real and imaginary parts of the potential. The bottom two are spin-orbit real and imaginary parts of the potential.

2.2 Microscopic Relativistic Description of Nucleon Nucleus Scattering

A number of relativistic approaches to nuclear physics suggests that the optical potential or self energy for a nucleon involves very large attractive Lorentz scalar and repulsive Lorentz vector contributions. Relativistic mean field calculations relate these potentials to large scalar and vector meson couplings and provide a good description of charge densities for closed shell nuclei [15]. Dirac optical model fits to elastic proton scattering also use strong potentials to reproduce analysing power data. Finally, relativistic impulse approximation (RIA) calculations find strong potentials coming from large scalar and vector pieces of a Lorentz invariant representation of the NN amplitudes. These RIA calculations provide an excellent description of elastic scattering at energies of 500 MeV and above [2].

Microscopic relativistic optical potentials have been calculated at energies near 200 MeV for elastic proton scattering from closed shell nuclei [7]. The 200 MeV energy region is interesting as a bridge between high energies, where the simple impulse approximation is valid, and between relativistic nuclear matter calculations. At this energy, one can ideally examine the medium modifications to the free NN interaction.

The Dirac optical potential for nucleon-nucleus elastic scattering is calculated in the following way. The relativistic Love-Franey parametrization [16] is used to calculate direct and exchange NN amplitudes $t_d(q)$ and $t_{ex}(Q)$, and these amplitudes are then folded with relativistic Hartree densities using a local density approximation for the exchange part to obtain the optical potential. Finally a correction factor is applied to include Pauli blocking [7].

This theory is essentially a modified RIA. It has three improvements: (a) medium modifications due to Pauli blocking are included, (b) pseudovector instead of pseudoscalar is assumed for πN coupling in the relativistic NN amplitude although both are in principle allowed, and (c) the exchange term, which arises from antisymmetrized wavefunctions, are explicitly treated in the optical potential. The present experiment serves as a good test of the Pauli blocking effect in the relativistic theory at this energy. We will not describe this theory in detail, but only roughly outline how the relativistic results have been calculated.

The relativistic model is based on the Dirac equation

$$[\vec{\alpha} \cdot \vec{p} + \beta(m + U_s) + U_v]|\phi >= E_i|\phi >$$

where only two Lorentz invariant potentials are used in the optical potential calculations, U_s, the scalar potential, and U_v, the vector potential. This equation is equivalent to a second order Schrödinger type differential equation for the upper component of the four-component nucleon-nucleus wave function which is obtained from the Dirac equation by standard techniques [19]. The final form of the equation for the upper component reads [20]:

$$\{\nabla^2 + k^2 - 2E[U_{eff}(r) - U_{so}(r)\vec{\sigma} \cdot \vec{L}]\}\Psi = 0$$

where k and E are proton-nucleus center-of-momentum wave number and total energy, respectively. The effective central(U_{eff}) and spin orbit(U_{so}) potential can be expressed in terms of the Dirac scalar(U_s) and vector (U_v) potentials. We neglect the unimportant tensor term.

$$U_{eff} = \frac{1}{2E}(2EU_v + 2mU_s - U_v^2 + U_s^2 + U_{DARW})$$

$$U_{so} = -\frac{1}{2E}\left[\frac{1}{rB}\frac{\partial B}{\partial r}\right]$$

where $B = (E + m + U_s - V_c)/(E + m)$; m is the proton mass and the Darwin term U_{DARW} is defined by

$$U_{DARW} = -\frac{1}{2r^2 B}\frac{\partial}{\partial r}\left(r^2\frac{\partial B}{\partial r}\right) + \frac{3}{4B^2}\left(\frac{\partial B}{\partial r}\right)^2$$

We have neglected the relatively small tensor Coulomb terms V_c^2 in our wave equation and the term V_c in B. The scalar and vector potentials are calculated from the relativistic Love-Franey NN interaction model [16].

2.2.1 Relativistic Love-Franey Model

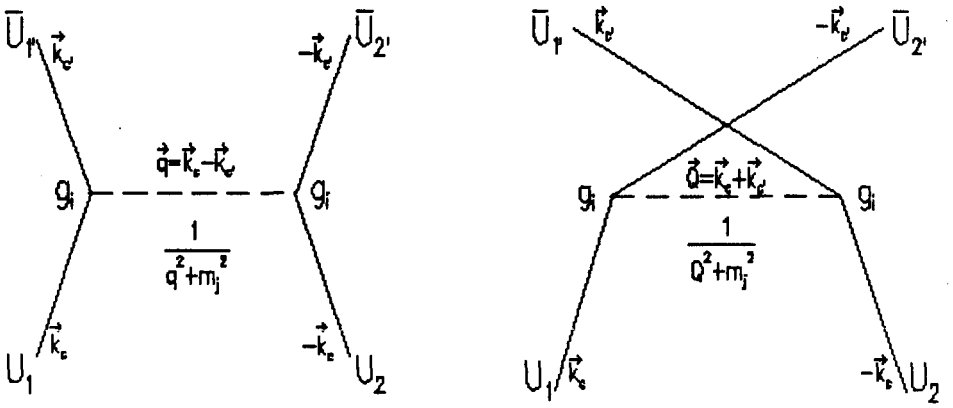

Figure 2.2: Feynman diagram of the NN interaction with direct (left) plus exchange (right) terms

The relativistic Love-Franey model of the NN interaction considers the exchange of a number of "mesons" in the first Born approximation including both the direct and exchange NN scattering diagrams (See Fig 2.2). The meson couplings and form factors are complex in order to generate the imaginary amplitude. They are adjusted until the relativistic representation of the Arndt amplitudes [23](which have been determined by fitting the NN scattering observables) is reproduced directly without iteration of the meson exchanged (Born approximation). This implies the neglect of the contributions

from mutiple meson exchange. The model assumptions about the relativistic form of the NN amplitudes are directly related to the type of meson-nucleon vertices used. Thus we can directly study the sensitivity of the resulting RIA optical potential to different vertices (e.g. the difference between pseudoscalar and pseudovector πN coupling). In addition, the parameters from the fit are very closely related to couplings of the one-boson-exchange potential(OBEP)[21]. Thus they have a direct physical meaning. Each of the five independent Lorentz invarant amplitudes (i.e. scalar, vector, pseudoscalar, pseudovector and tensor) can be associated with exchange of a different type of mesons (i.e. δ, B, π, ρ, f). Different types of mesons being exchanged produce the corresponding Lorentz invariant amplitude. The largest contributions come from the π, σ and ω. The model separation of the NN amplitude into direct and exchange contributions does not involve sensitive cancellations in contrast to the non-relativistic results [7]. In the following section we will show how these mesons produce the scattering amplitudes.

The Dirac optical potential is given by [34]

$$U_{opt} = \frac{-4\pi i p_{lab}}{m} < \psi|\hat{F}|\psi >$$

where p_{lab} is the lab momentum of the incident particle, $|\psi >$ is the ground state wavefunction of the target nucleus, usually constructed by a (Hartree) product of single particle wavefunctions (ϕ_α), and $\hat{F}$ is the relativistic scattering amplitude.

Each invariant F^i can be separated into direct and exchange parts, we get

$$\begin{aligned} F^i &= i\frac{E_{cm}}{2p_{cm}}[F^i_d(q) + F^i_{ex}(Q)] \\ &= t^i_d(q) + t^i_{ex}(Q) \end{aligned}$$

where q and Q are the momentum transfers in the direct and exchange diagrams, respectively. Thus the direct piece of the optical potential is [25]

$$U^i_d(r, E) = -\frac{4\pi p_{lab}}{m}\int d\vec{r'}\rho^i(r')t^i_d(|\vec{r} - \vec{r'}|, E)$$

The local density approximation in the nuclear matter approach was used to correct the finite nucleus optical potentials. This approximation was applied to incident and bound nucleon in the nonlocal exchange terms to arrive at the exchange piece of the potential [25]:

$$U^i_{ex}(r,E) = -\frac{4\pi p_{lab}}{m}\int d\vec{r'}\rho^i(r,r')t^i_{ex}(|\vec{r}-\vec{r'}|,E)j_o(k|\vec{r}-\vec{r'}|)$$

At low energy, exchange terms play a more important role in the calculation of the optical potential. Exchange terms have nonlocal properties, thus relativistic amplitudes must have nonlocal pieces which are lacking in the original RIA. A simple model with explicit exchange terms fitted to the relativistic amplitudes allows one to examine different off-shell extrapolations in the exchange terms.

Since the NN scattering data only determine the on-shell part of the NN amplitude whereas construction of the optical potential requires the full amplitude, one has to employ an explicit model of the NN amplitude to learn about its Lorentz structure and off-shell behavior. The on shell amplitude should reproduce the NN data. We start with relativistic scattering amplitude $\hat{F}$ which can be represented by a linear combination of five Lorentz invariants [7].

$$\hat{F} = \sum_{i=s}^{t}\lambda^i_1\lambda^i_2F^i \qquad \text{(i=s, v, p, a, t)}$$

where s=scalar, v=vector, p=pseudoscalar, a=axial vector and t=tensor. If the coupling constant for the ith meson is g_i, the meson propagator has the form $1/(q^2+m_i^2)$, and the nucleon form factor is $1/(1+\frac{q^2}{\Lambda_i^2})$. The NN interaction vertex from the Feynman rules is

$$\left(\frac{g_i\lambda^i}{1+\frac{q^2}{\Lambda_i^2}}\right)(\vec{\tau})^{I_i}$$

where i denotes the ith type of meson and $I_i = (0,1)$ is the meson's isospin. Adding scattering wave symmetry, the contribution of the ith meson to the amplitude, up to

overall kinematics factors, is [7]:

$$\overline{U}_{1'}\overline{U}_{2'}\hat{F}U_1U_2 \propto$$
$$\overline{U}_{1'}\left(\frac{g_i\lambda^i}{1+\frac{q^2}{\Lambda_i^2}}\right)U_1\frac{1}{m_i^2+q^2}\overline{U}_{2'}\left(\frac{g_i\lambda^i}{1+\frac{q^2}{\Lambda_i^2}}\right)U_2(\vec{\tau}_1\cdot\vec{\tau}_2)^{I_i}$$
$$+(-1)^T\overline{U}_{2'}\left(\frac{g_i\lambda^i}{1+\frac{Q^2}{\Lambda_i^2}}\right)U_1\frac{1}{m_i^2+Q^2}\overline{U}_{1'}\left(\frac{g_i\lambda^i}{1+\frac{Q^2}{\Lambda_i^2}}\right)U_2(\vec{\tau}_1\cdot\vec{\tau}_2)^{I_i}$$

From the Feynman rules, it is quite straightforward to write down the direct contributions.

$$F_d^i(q)=\sum_{j=1}^{N}\delta_{i,j}(\tau_1\cdot\tau_2)^{I_i}f^i(q)$$

where j stands for the type of mesons, $f^j(q)$ contains form factors, coupling constants and the propagator,

$$f^j(q)=f_R^j(q)-if_I^j(q)$$

$$f_R^j(q)=\frac{g_j^2}{q^2+m^2}(1+q^2/\Lambda_j^2)^{-2}$$

$$f_I^j(q)=\frac{\overline{g}_j^2}{q^2+\overline{m}^2}(1+q^2/\overline{\Lambda}_j^2)^{-2}$$

where m_j is the meson mass and g_j,Λ_j are fitted to the data. The imaginary part is also fitted to the data to determine the parameters $\overline{m},\overline{g}_j,\overline{\Lambda}_j$. Similar formula were obtained for the exchange terms:

$$F_{ex}^i(Q)=(-)^{I_{NN}}\sum_{j=1}^{N}C_{i,j}(\tau_1\cdot\tau_2)^{I_j}f^j(Q)$$

where $C_{i,j}$ is the Fierz matrix [7] and I_{NN} is the isospin of the two nucleon state. Finally the isospin states are combined to get the pp and pn amplitudes.

$$F^i(pp)=F^i(I_{NN}=1)$$

$$F^i(pn)=F^i(I_{NN}=1)+F^i(I_{NN}=0)$$

The resulting coupling constants are remarkably close to OBEP results and have very little energy dependence. The coupling constants show that π exchange provides most of the attractive interaction while σ gives most of the repulsive interaction [7]. This conclusion agrees with OBEP results [21].

The πN vertex can be represented by either

$$\overline{\psi}\gamma_5\psi\phi \qquad \text{Pseudoscalar}$$

or

$$\overline{\psi}\gamma_5\gamma_\mu\psi\partial^\mu\phi \qquad \text{Pseudovector}$$

This choice does not affect the on-shell amplitudes, but has some effects on-off shell elements. Since NN experimental data only determine the on-shell elements, either choice is compatible with the simple RIA [2]. The choice of using pseudoscalar and pseudovector πN couplings affects the exchange contribution. The pseudovector coupling reduces the potential by a factor of $\pm Q^2/4M^2$. It is easy to see how this factor arises, since $\partial_\mu\phi = \frac{q}{2M}\phi$ and the amplitude is just the square of this factor. This factor is much less than one which prevents the optical potential from diverging at low energy in good agreement with phenomenological fits.

The optical potential for proton scattering from spherical nuclei with the impulse approximation is given by Lorentz scalar and vector components [7].

$$\begin{aligned} U_{opt} &= -4\pi i[\frac{p}{M}](F^s\rho_s + \gamma^0 F^v\rho_v) \\ &= U^s + \gamma_o U^v \end{aligned}$$

where ρ_s and ρ_v are scalar and vector density respectively. They are defined by

$$\rho_s = \sum_\alpha^{occ} \overline{\phi}_\alpha\phi_\alpha$$

$$\rho_v = \sum_{\alpha}^{occ} \phi_\alpha^\dagger \phi_\alpha$$

where ϕ_α is the single particle wavefunction for occupied nuclear levels.

The optical potential can be broken into direct and exchange pieces

$$U_{opt} = U_d(r, E) + U_{ex}(r, E)$$

The direct amplitude does not contribute to the optical potential. The scalar and vector exchange potentials can then be projected out by taking traces.

$$U_v = \frac{4\pi p_{lab}}{m}\left(\frac{m^2}{2E_c k_c}\right) f^P(Q) \frac{3}{8} \frac{(2Q_o^2 - Q_\mu^2)}{4m^2} \rho_v$$

$$U_s = \frac{4\pi p_{lab}}{m}\left(\frac{m^2}{2E_c k_c}\right) f^P(Q) \frac{3}{8} \left(-\frac{Q_\mu^2}{4m^2}\right) \rho_s$$

Here the Dirac scalar and vector potentials are expressed in terms of scalar (ρ_s) and vector (ρ_v) densities and the scalar and vector NN invariant amplitudes. The amplitudes were obtained by fitting the NN phase shifts [23], the scalar and vector densities were provided by relativistic Hartree calculations [15].

The potential including the Pauli blocking correction is related to the uncorrected potential by

$$U_{pb}^i(r) = [1 - a_i(T_{lab}) \left(\frac{\rho_b(r)}{\rho_o}\right)^{\frac{2}{3}}] U^i(r)$$

where $\rho_o = 0.1934 fm^{-3}$ and the a_i are Pauli blocking factors calculated from a nuclear matter approach [21]. It turns out that at 200 MeV the imaginary potentials are reduced by about 10% while the effect on the real potential is smaller.

2.3 Differences between non-relativistic and relativistic models

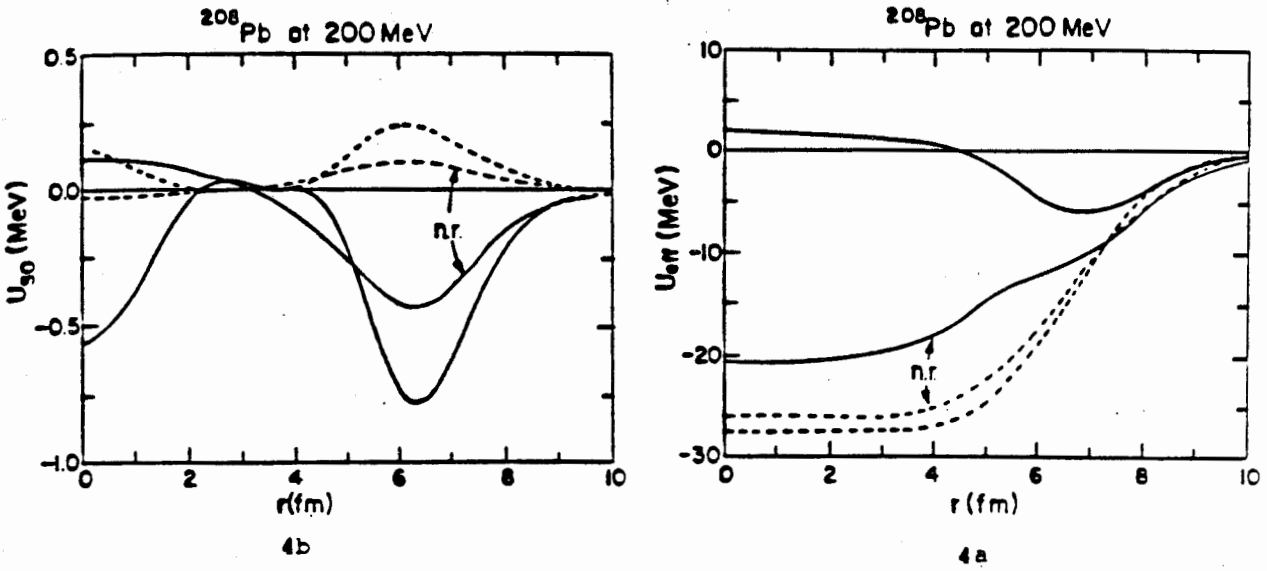

Figure 2.3: Relativistic and Schrödinger potentials for ^{208}Pb at 200 MeV. Relativistic calculations are compared with the nonrelativistic (n.r.) results of Von Geramb. Real potentials are solid and imaginary dashed curves.

1) The relativistic real central potential has a non-Wood-Saxon shape. It is composed of two pieces which are much stronger than commonly used nonrelativistic potentials and is quantitatively different from the latter (See Fig 2.3). The nonrelativistic real central potential also has a non-Wood-Saxon shape. It looks like a superposition of two Wood-Saxon form factors with different parameters.

2)In relativistic calculations, the Pauli blocking is included in a simple way, no exact calculation is done and potential is parameterized by a factor. In the nonrelativistic case, Pauli blocking is built into the interaction from the very beginning.

3) The amount of medium modification included is different in the two approaches. Non-relativistic theory includes the Fermi motion, binding energy corrections and Pauli

blocking, while in the relativistic case only Pauli blocking is so far included. The present work provides a good test of whether the relativistic effects or medium modification should play an important role in nucleon-nucleus elastic scattering.

Chapter 3

Experiment

In the first part of this chapter, we describe the experimental apparatus and its function in the experiment. In the second part we discuss details of the data analysis.

3.1 TRIUMF Site

The main components of the TRIUMF site are the cyclotron, the beam lines and the experiment areas. The TRIUMF six sector cyclotron can produce polarized or unpolarized proton beams with continuously variable energies between 180 and 520 MeV. The ion source produces an H^- beam for injection into the cyclotron. The polarized beam for this experiment was produced by an atomic beam ion source, a 'conventional' polarized ion source, utilizing Stern-Gerlach separation of atoms with given electronic spin projection, followed by appropriate RF transitions and electron attachment to the H atoms by electron bombardment. The direction of the polarization can be reversed by selecting different RF transitions. Extraction of the beam from the cyclotron is done by passing part or all of the H^- beam through a stripper foil, creating protons which bend out of the cyclotron into the beam line. The location of the stripper can

be adjusted radially to provide a continuously variable beam energy. The beam line consists of focusing quadrupoles and bending dipole magnets which transport the beam into the experimental area. Our experiment was carried out on beam-line 4 (BL4B) in the proton hall.

3.2 Experimental Apparatus

Our detection system consists of five main parts (See Fig 3.1):

1. A superconducting solenoid magnet is used to rotate the vertical polarization of the incident beam in the desired sideways direction by setting up a current of the required polarity in the solenoid.

2. An in-beam-polarimeter (IBP) which allows continuous measurement of the beam polarization.

3. A beam twister, consisting of six quadrupoles, was used to rotate the beam dispersion direction from the horizontal to the vertical direction for the purpose of dispersion matching.

4. A target chamber (4BT2) which contains the primary target foils.

5. The medium resolution spectrometer (MRS). This is the central part of the detection system. It measures momentum spectra of the scattered particles.

6. The focal plane polarimeter(FPP) which measures the transverse polarization components of the scattered protons after the focal plane of the MRS.

Here I briefly describe each part of the experimental system and its function. The superconducting solenoid function has already been discussed above.

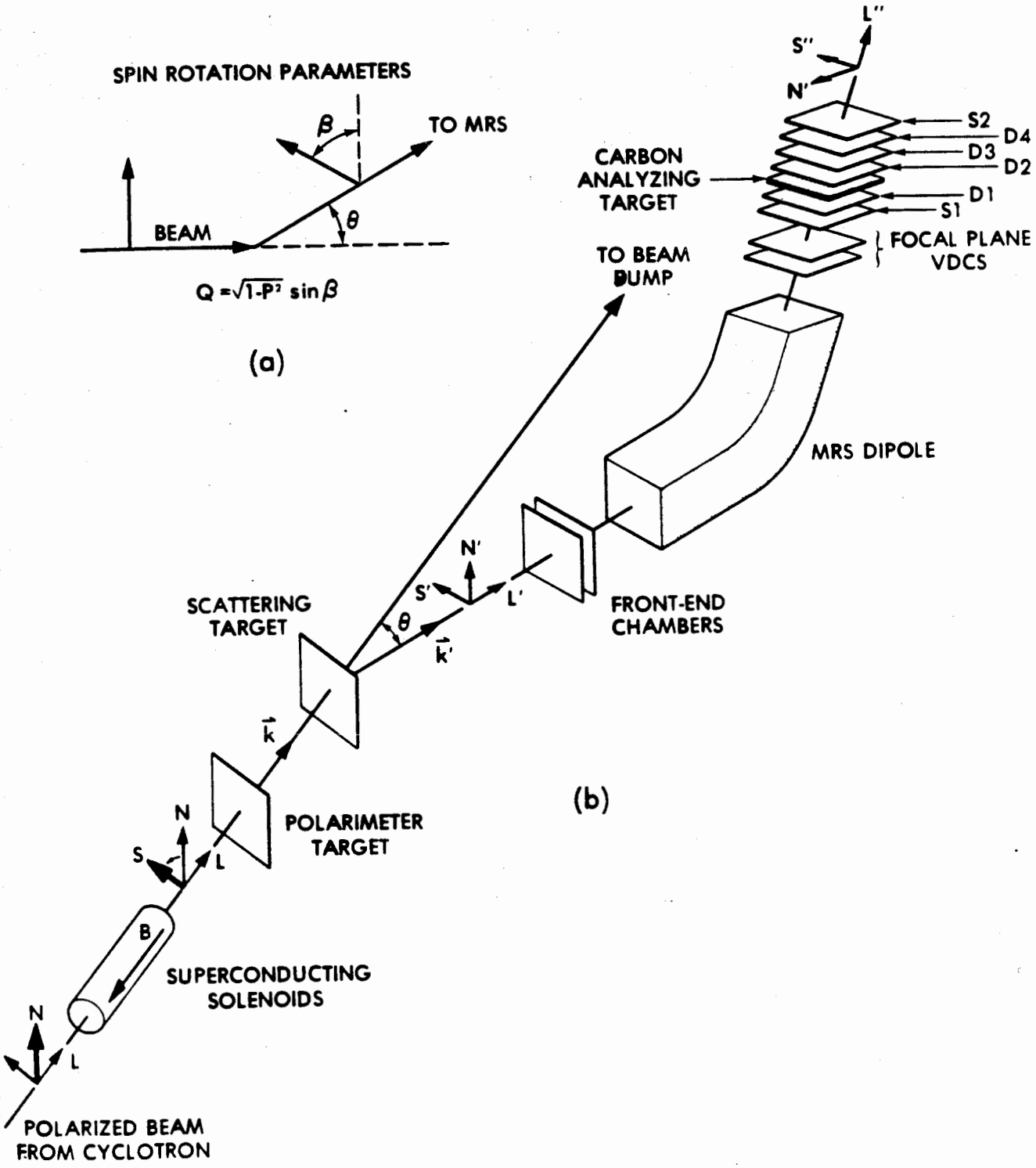

Figure 3.1: Experimental layout and principle of measurement

The IBP was used to monitor beam polarization [22]. It consists of four detector telescopes which detect both particles from pp scattering in a CH_2 target at $\theta_{lab} \sim 17°$. At 200 MeV the proton beam polarization was measured with an effective CH_2 analyzing power of 0.234. One of the two detector systems determines the top-bottom asymmetry, the other two yield the left-right asymmetry.

The function of the twister, a unit section of six quadrupoles, is to rotate the beam dispersion direction by 90°, so that the beam becomes vertically dispersed (originally horizontally dispersed) for the purpose of dispersion matching. Calculations of the dispersed beam tune for 4BT2 must take into account the precession solenoid which also rotates the phase space of the beam. This has the effect that the twister rotation angle changes from 45° to either 37° or 53° (depending on solenoid polarity) to achieve vertical dispersion at T2.

The target ladder contained the target foils of interest (^{208}Pb , ^{90}Zr , CH_2) and a ZnS scintillator screen. Target changes can be made remotely.

The MRS is located at target station T2 of beam line 4B. It consists of a focusing quadrupole, a 60° vertical-bend dipole magnet and a detector system. The front-end wire chambers(FEC) and two vertical drift chambers near the focal plane are used to determine particle trajectories. A set of plastic scintillators measures the energy loss of particles, and serves together with the counters at the entrance of the MRS as a trigger and also provides time of flight information for particle identification. Another function of these trigger paddles is to define the effective momentum acceptance of the spectrometer. We turned off trigger paddles and used a veto scintillator to eliminate the continuous part of the spectrum. The FECs allow us to ray-trace protons back to the target and to define the spectrometer solid angle. Solid angles of the MRS of the order 0.5 to 2 msr were used. The momentum acceptance of the MRS is about $\pm 7\%$ for

particle momenta up to 1.5 GeV/c. Scattering angles range from $-12°$ to $+135°$.

The most important part of the detector system is the FPP [24]. It consists of (1) four wire chambers (D1—D4), and (2) as many as four carbon slabs,(3) a trigger scintillator in front of the scatterer and a large trigger scintillator at end of the FPP cage. The FPP uses inclusive scattering from carbon slabs which are mounted after the focal plane of the MRS. Particle trajectories were determined by means of the wire chambers. Both independent components of polarization normal to the particle trajectory are measured. A high efficiency for nuclear scattering is achieved by using carbon scatterers as thick as possible, subject to multiple scattering limitations. The four drift chambers measure scattering angles at all azimuthal angles out to polar angles of 20° over a spectrometer momentum acceptance of $\pm 5\%$. A microprocessor rejects events with small scattering angles.

The requirement that the polarimenter not interfere with normal high resolution operation of spectrometer implies that the polarimeter had to be placed after the focal plane detectors (vertical drift chamber and trigger scintillators). Usually the focal plane is located just below VDC1; it is oriented at 45° to the optical axis, parallel to the VDC's.

Particles are tracked through the polarimeter using position information from the four multi-wire chambers, each consisting of a "x" and a "y" plane with delay-line readout to identify the cell number. Alternate anode and cathode wires form drift cells 8.13 mm wide. The anode wires are connected directly to a low loss delay line having a signal propagation speed of 0.4cm/ns. Each cathode wire is connected to one of two buss lines depending upon whether it is an "odd" or "even" wire. The difference in times at which signals reach two ends of the delay line determines the cell number, while their average depends on the drift time and hence on the distance of a particle track from the nearest anode wire. The ambiguity in the direction of drift was solved by

observing the charge induced in "odd" and "even" cathode sense wires [26]. We encode three timing signals: TDC time for each end (left and right) of the delay line (T_l, T_r), as well as T_c, the cathode timing signal. Also encoded are the ADC amplitudes of the two cathode signals, E_{odd} and E_{even}. From these data we generate:

1. The anode wire position, $T_l - T_r$.
2. The drift time T_d from the anode timing, $T_l + T_r = 2T_d + T$ where T, the total drift time through the whole delay line, is a constant
3. A checksum spectrum, $T_l + T_r - 2T_{d'} = 2(T_d - T_{d'}) + T$=constant
4. A normalized cathode difference spectrum, $(E_{odd} - E_{even})/(E_{odd} + E_{even})$.

The polarimeter trigger system consisted of two plastic scintillators, one after the first drift chamber but before the carbon scatterer (S1), and the other after the three chambers following the carbon (S2). Signals from S1 and S2 coincidences provide a local trigger for the polarimeter, as well as the time reference for drift chambers. Events of interest in a polarimeter are those in which the normal spectrometer coincidence condition("MRS") is met, as well as the coincidence in the polarimeter trigger ("FPP").

The checksum spectrum contains a sharp peak for 'good' events and is used for rejection of multiple events in a wire plane. Two nearly coincident avalanches in a wire plane can cause the T_l and T_r stop signals to come from different avalanches. This can look like a single event in a third position but appears outside the peak in the checksum spectrum.

A event microprocessor is used to reject large fractions of small angle scatterings occuring in the carbon analyser. Fewer than one particle in ten are scattered in the polarimeter through a polar angle large enough to be useful, whereas the majority of

small angle multiple scattering events have an analyzing power of essentially zero. To eliminate the overhead of transfering useless data along the CAMAC branch, a small angle test is performed by the microprocessor. It reads the data from the TDC's and tests whether the event is "good" or "bad". "Good" data are passed to the MRS data acquisition computer, while for "bad" events a "fast clear" signal is issued to the FPP and MRS electronics.

"Good" events are (1) pulse generated test events, (2) software prescaler test events to accumulate 1 of n events unconditionally, or (3)events which have passed tests for scattering angle and collinearity, plus check-sum tests for each plane. The combination $X_1 - 2 \cdot X_2 + X_4$ (where X_n is the bend plane coordinate in wire chamber n, and similarly for the y direction) is zero if no scattering occured in the carbon, and is used as crude measure of the scattering angle. If the sum of squares of deviations in the x and y direction is less than a specified amount the event is rejected as "bad" (small-angle scattering). The checksum test is applied to each plane to eliminate multiple-track events. Finally a straight line test is applied to the x and y coordinates for chambers 2, 3 and 4. It is intended to eliminate events for which a large-angle scattering occured between chambers and also events in which a false multiple track passed the checksum test. This can happen if the "false" track had a much shorter drift time than the true track, so that its signal reached both ends of the delay line first. The most common cause of an event being rejected is that the scattering angle is too small.

For good events the FPP data are buffered in microprocessor memory, and the MRS VDC data in the memory of its CAMAC interface unit. While these buffered data are being read by the MRS data acquisition computer the system is free to respond to subsequent triggers and reject or accept events.

Pulser-generated events were used to monitor the deadtime of the computer. Triggers were derived from random coincidences between a pulser and the signal from the IBP to ensure that the pulser event rate is proportional to the beam current. This procedure is essential for a correct sampling of the deadtime. We note that deadtime and beam normalization are of secondary importance in the FPP experiment since the crucial information is derived from the azimuthal variation in the yield as observed with the FPP.

Since spectrum resolution was not important in the present experiment, we omit the discussion of the dispersion matching.

We note that two distinctly different mechanical modes exist depending on whether small angles (SAC range from $3^\circ \sim 15^\circ$) or large angles (LAC $16^\circ \sim 135^\circ$) are to be measured.

Chapter 4

Data Reduction

In this chapter we describe the definition and measurement of Q, the procedures used for online data acquisition and for off-line analysis of taped events. Computer programs used to extract the spin observables are also discussed.

4.1 Definition and Measurements of Q

In this section, I briefly explain the principle of our experiment and how spin observables were measured.

We first define coordinate systems in which the scattering process can be easily and completely described. There are three coordinate systems in our analysis. The first is the beam line system labeled as $(\hat{s}, \hat{n}, \hat{l})$. This frame is used to define the beam polarization. Since the MRS front end chamber is in the horizontal plane, it only takes the events that have $\vec{K_f}$ in this plane. Thus $\hat{n} = (\vec{K_i} \times \vec{K_f})/|\vec{K_i} \times \vec{K_f}|$ is always in the vertical directon. $\hat{l}$ is chosen along the momentum direction of the incident beam, that is $\vec{K_i}/|\vec{K_i}|$. $\hat{s}$ is defined to form a right hand system with $\hat{n}$ and $\hat{l}$. This frame is also called the incident helicity frame. The second system is the scattered particle frame given by

$(\hat{s}', \hat{n}', \hat{l}')$ with $\hat{n}' = \hat{n}$, $\hat{l}'$ along $\vec{K}_f$ and $\hat{s}' = \hat{n}' \times \hat{l}'$. The actual scattering process is defined in terms of this frame. The final frame employed describes the polarization at the second scattering in the FPP. This focal plane frame is denoted by $(\hat{s}'', \hat{n}'', \hat{l}'')$ with $\hat{n}'' = \hat{n}', \hat{l}''$ along the momentum direction of the protons after their bending in MRS magnet and $\hat{s}''$ is chosen to form a right hand frame. The two transverse components of polarization, $P_{n''}$ and $P_{s''}$ are measured in this frame.

In elastic scattering, the proton polarization vector does not change amplitude, instead it changes orientation. Q is related to the rotation angle β, which is defined as the angle between the projection of the incoming proton spin and outgoing proton spin in the scattering plane, by the expression $Q = \sqrt{1 - P^2} \sin\beta$. We can not measure Q directly, instead we measure the Wolfenstein parameters which are also related to the spin rotation through $Q = -D_{sl'} \cos\theta_{lab} + D_{ss'} \sin\theta_{lab}$. The Wolfenstein parameters can be calculated from the polarization components after scattering. In the experiment a sideways polarized beam is used and polarization components $P_{s'}$ and $P_{l'}$ are determined by measuring the azimuthal asymmetry in the focal plane polarimeter(FPP)[24]. Although we can't measure the longitudinal polarization component directly, the precession of the proton spin in the magnetic field of the MRS dipole makes this possible. It converts about 76% of the longitudinal component into the normal direction. Thus the longitudinal polarization of the scattered protons can be measured. Separation of the $P_{l'}$ and $P_{n'}$ components is achieved by flipping the spin of the incident beam, $P_{l'}$ will change sign while $P_{n'}$ will not.

This method is capable of determining the unknown longitudinal components which may exist in the incident beam. By using different combinations of spin of the incident beam (up and down) and solenoid currents (+ and −), we can extract the longitudinal polarization in the incident beam. A fifth independent measurement uses the unpolar-

ized beam. From a total of ten independent measurements (combination of spin up , down, and off with solenoid polarity +, −) of $P_{s''}$ and $P_{n''}$ combined with transverse polarization results measured by the IBP, we derive four independent quantities: the polarization of the scattered protons, the spin transfer coefficients $D_{ss'}$ and $D_{sl'}$ and the longitudinal polarization component of the incident beam (P_l). In the following section I give a detailed derivation of these quantities.

This experiment is a double scattering experiment. The first scattering occurs at the target of our interest, whereas the second scattering in the FPP serves to analyse the polarization of protons scattered from the primary target. A carbon analyser was used for the analysis of the polarization after scattering. Nuclear scattering is the only method available for measuring the polarization of a beam of particles in the intermediate energy regime.

4.1.1 Description of Polarization

A spin 1/2 particle can be represented by a 2-component spinor:

$$\chi = \begin{bmatrix} a_1 \\ a_2 \end{bmatrix}$$

It is convenient to define the density matrix as

$$\rho = \chi\chi^\dagger = \begin{bmatrix} |a_1|^2 & a_1 a_2^* \\ a_2 a_1^* & |a_2|^2 \end{bmatrix}$$

Then any physical observables measured in this state (expectation value) would be simply [27]

$$< U >= \chi^\dagger U \chi = Tr(U\chi\chi^\dagger) = Tr(U\rho)$$

The state of polarization is specified by the Pauli spin operators $\sigma_x, \sigma_y, \sigma_z$, the corresponding expectation values are

$$p_x =< \sigma_x >= 2Re(a_1 a_2^*)$$

$$p_y =< \sigma_y >= 2Im(a_1 a_2^*)$$

$$p_z =< \sigma_z >= (|a_1|^2 - |a_2|^2)$$

The set of operators $I, \sigma_x, \sigma_y, \sigma_z$ form a complete set of Hermitian matrices for the 2×2 space. Any operator in this space must be a linear combination of these operators. If we define $\sigma_0 = I, \sigma_1 = \sigma_x, \sigma_2 = \sigma_y, \sigma_3 = \sigma_z$, then we have (orthogonality relation)

$$Tr(\sigma_i \sigma_j) = 2\delta_{ij}$$

where i, j=0,1,2,3. The density matrix is one of the operators in this space and can be written as

$$\rho = \sum_j a_j \sigma_j$$

Using the orthogonality relation, it can be shown that

$$\rho = \frac{1}{2}(I + \sum_{j=1}^{3} p_j \sigma_j)$$

The outgoing particle spinor can be related linearly to the incoming particle spinor by

$$\chi_f = M \chi_i$$

where M is a 2×2 matrix whose elements are functions of energy and angle, and i and f denote 'initial' and 'final', respectively. χ_i and χ_f may be defined in different coordinate systems. For most of the present discussion we will use the incident helicity frame and the scattered particle frame.

Using the definition of the density matrix and the relation between the initial state and the final state, it is easy to show that

$$\rho_f = M\rho_i M^\dagger$$

where M is the scattering matrix. If ρ_i is normalized, then the differential cross section for a polarized beam is given by

$$\begin{aligned} I(\theta,\phi) &= Tr\rho_f \\ &= Tr(M\rho_i M^\dagger) \\ &= I_o(\theta)(1+\sum_{j=1}^{3} p_j A_j(\theta)) \end{aligned}$$

where

$$A_j(\theta) = \frac{Tr(M\sigma_i M^\dagger)}{Tr(MM^\dagger)}$$

is the analysing power of the reaction for the j'th initial polarization component and $I_o = \frac{1}{2}Tr(MM^\dagger)$ is the differential cross section for a unpolarized incident beam. Conceptually the analysing power is a function of energy and angle for a particular target.

To calculate the polarization of the scattered particle, we must use a normalized density for the final state so that

$$\begin{aligned} p_{k'} &= <\sigma_{k'}> = \frac{Tr(\rho_f\sigma_{k'})}{Tr\rho_f} \\ &= \frac{1}{2I}\left[Tr(MM^\dagger\sigma_{k'}) + \sum_{j=1}^{3} p_j Tr(M\sigma_j M^\dagger\sigma_{k'})\right] \\ &= \frac{I_o}{I}(P_{k'}(\theta) + \sum_{j=1}^{3} p_j K_j^{k'}) \end{aligned}$$

where

$$P_{k'} = \frac{Tr(MM^\dagger\sigma_{k'})}{Tr(MM^\dagger)} \qquad K_j^{k'}(\theta) = \frac{Tr(M\sigma_j M^\dagger\sigma_{k'})}{Tr(MM^\dagger)}$$

$P_{k'}$ is the k'th component of polarization which would be produced by an unpolarized beam, and $K_j^{k'}$ is the polarization transfer coefficient that relates the jth initial com-

ponent to k'th final polarization component. All of the polarization observables vary between +1 and -1. The quantities $P_{x'}, P_{y'}$ and $P_{z'}$ are of a similar character to the analysing power, and for an unpolarized beam the equality holds

$$p_{k'} = P_{k'}$$

For a polarized beam $P_{k'}$ is not separately associated with the properties of the system.

The quanlities $K_i^{j'}$ are identical to the Wolfenstein D parameters and , if the x', y', z' coordinate system is specified to be the scattered particle frame,

$$K_x^{x'} = D_{ss'} \quad K_z^{x'} = D_{ls'} \quad K_z^{z'} = D_{ll'} \quad K_x^{z'} = D_{sl'}$$

The remaining K are zero if parity is conserved.

It can be shown that when parity conservation and time reversal invariance are applied to the elastic scattering of a nucleon from a spin zero target, we obtain the following relations [27]:

$$A_y = P_y \qquad D_{ss'} = D_{ll'} \qquad D_{sl'} = -D_{ls'} \qquad D_{nn'} = 1$$

$$A_y^2 + D_{ss'}^2 + D_{ls'}^2 = 1$$

where P is the induced polarization or simply polarization. The scattering matrix can be written

$$M = A + B\sigma_y = \begin{bmatrix} A & -iB \\ iB & A \end{bmatrix}$$

where y is the direction normal to the scattering plane. There are three independent quantities in this matrix. The overall phase factor has no physical significance. The cross section and analyzing power determine two of these quantities,

$$\sigma = |A|^2 + |B|^2$$

$$A_y = \frac{2Re(A^*B)}{|A|^2 + |B|^2} = P$$

It is natural to define the third parameter as

$$Q = \frac{2Im(A^*B)}{|A|^2 + |B|^2}$$

We now introduce the spin rotation angle as follows:

When a polarized spin 1/2 particle is scattered from a spin 0 target, the component of polarization in the scattering plane will be rotated through some angle (β) called the spin rotation angle β.

A detailed calculation shows that Q is directly related to this angle through $\sqrt{1-P^2}\sin\beta$ where P is the induced polarization (see below). Here I give a simple derivation of the spin rotation parameter Q showing how this parameter is related to the spin rotation angle (β). For elastic scattering, we may use one frame of reference to describe the incoming and outgoing particle (beam line frame) or we may use the outgoing scattered particle frame for scattered protons. In both cases, the $\hat{e}_y$ vector is defined to be in the normal direction of the scattering plane. It has been shown that in both frames the final polarization is related to the initial polarization (in the beam line system) by [28] [27]

$$\vec{P}' = \begin{bmatrix} P'_s \\ P'_n \\ P'_l \end{bmatrix} = \left\{ \begin{bmatrix} D_{ss} & 0 & -D_{sl} \\ 0 & 1 & 0 \\ D_{sl} & 0 & D_{ss} \end{bmatrix} \vec{P}_b + \begin{bmatrix} 0 \\ P(\theta) \\ 0 \end{bmatrix} \right\} \frac{1}{1 + P_n A_y}$$

One notices that the normal polarization component does not transfer to other direction. Thus as long as the $\hat{y}$ direction of a new frame coincides with that of the scattering plane, this relation also holds for that frame except that the D coefficients will be transformed by a rotation. For example, for the final polarization measured in the scattered particle frame we have:

$$\begin{bmatrix} D_{ss'} \\ D_{ls'} \end{bmatrix} = \begin{bmatrix} \cos\theta & \sin\theta \\ -\sin\theta & \cos\theta \end{bmatrix} \begin{bmatrix} D_{ss} \\ D_{ls} \end{bmatrix}$$

The components of polarization in the scattering plane for incident particle and outgoing particle are

$$\vec{P}_{\|} = P_s\hat{e}_s + P_l\hat{e}_l \qquad \vec{P}'_{\|} = P_{s'}\hat{e}_{s'} + P_{l'}\hat{e}_{l'}$$

The tangent angle of these vectors with respect to $l(z)$ axis are simply

$$\tan\phi = \frac{P_s}{P_l} \qquad \tan\phi' = \frac{P_{s'}}{P_{l'}}$$

The spin rotation angle can now be expressed in terms of these two tangents

$$\tan\beta = \tan(\phi' - \phi) = \frac{\tan\phi' - \tan\phi}{1 + \tan\phi'\tan\phi} = \frac{P_{l'}P_s - P_lP_{s'}}{P_lP_{l'} + P_sP_{s'}}$$

Substituting for P' in terms of P, we obtain

$$\tan\beta = \frac{D_{ls}}{D_{ss}} \quad \text{or} \quad \sin\beta = \frac{D_{ls}}{\sqrt{D_{ss}^2 + D_{ls}^2}}$$

A detailed calculation shows [27] that

$$D_{ls} = \frac{2Im(A^*B)}{|A|^2 + |B|^2}$$

which is just the spin rotation parameter. Since we have the quadratic relation:

$$D_{ss'}^2 + D_{sl'}^2 + P^2 = D_{ss}^2 + D_{sl}^2 + P^2 = 1$$

We can rewrite $\sin\beta$ as

$$\sin\beta = \frac{D_{ls}}{\sqrt{1-P^2}} = \frac{1}{\sqrt{1-P^2}}(D_{ss'}\sin\theta - D_{sl'}\cos\theta)$$

The last factor is our spin rotation parameter, thus

$$Q = \sqrt{1-P^2}\sin\beta$$

In our experiment we measure $D_{sl'}$ and $D_{ss'}$, which allows us to derive Q.

4.2 Beam Polarization

In our experiment we have four modes of running. Two with beam polarization up and down, two with opposite current polarities of the superconducting solenoid magnet positive and negative (denoted P and M). The solenoid precesses the proton spin by 90° clockwise or counterclockwise depending on the direction of the current in the magnet. The beam delivered to beam line 4B is essentially polarized in the normal (vertical) direction, i.e. $P_n >> P_l, P_s$.

We will see that only the relative sign between different modes of beam polarization is important. Let $P_m^{\uparrow}$ be the beam polarization after the solenoid with the initial beam spin up and the solenoid polarity negative. If we assign its form as

$$P_m^{\uparrow} = \begin{bmatrix} P_s \\ P_n \\ P_l \end{bmatrix}$$

Then in the other cases, (with spin up, the solenoid positive and spin down, the solenoid negative and positive) the relative signs of the polarizations would be:

$$P_p^{\uparrow} = \begin{bmatrix} -P_s \\ -P_n \\ P_l \end{bmatrix} \quad P_m^{\downarrow} = \begin{bmatrix} -P_s \\ -P_n \\ -P_l \end{bmatrix} \quad P_p^{\downarrow} = \begin{bmatrix} P_s \\ P_n \\ -P_l \end{bmatrix}$$

where $P_s >> P_n, P_l$.

The beam polarization was primarily monitored by an in-beam polarimeter(IBP) [22]. The average beam polarization during our experiment runs was fairly stable ($|\vec{P}| \sim 0.76$) for all 4 different conditions. During a few runs, depolarization occured due to cyclotron detuning. However since our analysis is based on a run-by-run basis, the variations in polarization of the incident beam polarization do not affect the final results.

If the incident proton beam has polarization $\vec{p}$, the cross section for scattering from a H nucleus in the IBP can be written as

$$\sigma(\theta, \phi) = \sigma_o(1 + \mathrm{A_y}(\theta)\vec{\mathrm{p}} \cdot \vec{\mathrm{n}})$$

where I_0 is the cross section for scattering of an unpolarized beam into the scattering angle θ, $A(\theta)$ is the analysing power of the reaction, and $\vec{n}$ is the unit vector of the scattering plane defined by the cross product of the incident momentum and outgoing momentum ($\vec{k}_{in} \times \vec{k}_{out}$). In the beam line frame $\vec{n} = (-\sin\phi, \cos\phi, 0)$ thus

$$\begin{aligned} \sigma(\theta,\phi) &= \sigma_o(1 - \mathrm{P_s A_y}(\theta)\sin\phi + \mathrm{P_n A_y}(\theta)\cos\phi) \\ &= \sigma_o(1 + \varepsilon_s \sin\phi + \varepsilon_n \cos\phi) \end{aligned}$$

It follows that

$$\varepsilon_s = -P_s A_y(\theta) \qquad \varepsilon_n = P_n A_y(\theta)$$

If we define left (right) cross section $\sigma_L(\sigma_R)$ measured by the left (right) detector telescope arm in the IBP as

$$\sigma_L = \sigma(\phi = 0°) = \sigma_o(1 + \mathrm{P_n}) \qquad (\sigma_R = \sigma(\phi = 180°) = \sigma_o(1 - \mathrm{P_n}))$$

Then the normal components of the beam polarization can be derived from above two equations

$$P_n = \frac{1}{A_y(\theta)} \frac{\sigma_L - \sigma_R}{\sigma_L + \sigma_R}$$

In a similar way, we derive the sideways component of the beam polarization as:

$$P_s = -\frac{1}{A_y(\theta)} \frac{\sigma_T - \sigma_B}{\sigma_T + \sigma_B}$$

where we assume that the top (bottom) cross section is defined by

$$\sigma_T = \sigma(\phi = 90°) = \sigma_o(1 - \mathrm{P_s}) \qquad (\sigma_B = \sigma(\phi = 180°) = \sigma_o(1 + \mathrm{P_s}))$$

We assume there can be some inherent asymmetry in the IBP, (this may be caused by improper beam centering on the CH_2 target of the IBP, for example). With unpolarized beam, we measure only

$$\sigma_L = \sigma_o[1 + \varepsilon_a] \qquad \sigma_R = \sigma_o[1 - \varepsilon_a]$$

where ε_a is the inherent asymmetry of the IBP. From this we can determine the asymmetry of the IBP.

$$\varepsilon_a = \frac{\sigma_L - \sigma_R}{\sigma_L + \sigma_R}$$

Now if we have a polarized beam, the left(right) detector will measure cross sections as

$$\sigma_L = \sigma_o[1 + PA_y][1 + \varepsilon_a] \qquad (\sigma_R = \sigma_o[1 - PA_y][1 - \varepsilon_a])$$

where P is the beam polarization and A_y is the effective analysing power of the IBP target.

We can now calculate the normal beam polarization. (A similar expression holds for sideways polarization.)

$$P_n = \frac{1}{A_y} \frac{\sigma_L(1 - \varepsilon_a) - \sigma_R(1 + \varepsilon_a)}{\sigma_L(1 - \varepsilon_a) + \sigma_R(1 + \varepsilon_a)}$$

In the analysis, we calculated the beam polarization in two ways. The first uses an effective analysing power of CH_2 for the IBP target A_y. The second uses the H analysing power and corrects for the carbon content in the IBP target (carbon subtraction). Both methods give the same result as would be expected. The average polarization of the $\hat{s}$-type incident beam on the target was 0.763.

4.3 The Scattering Process

Assume that the polarization of the incident beam in the beam line system (also in the incident helicity frame)$(\hat{s}, \hat{n}, \hat{l})$ is given by a vector

$$\vec{P}_b = \begin{bmatrix} P_s \\ P_n \\ P_l \end{bmatrix}$$

After scattering from the primary target, the polarization in the scattering particle system $(\hat{s}', \hat{n}', \hat{l}')$ is given by

$$\vec{P}' = \begin{bmatrix} P'_{s'} \\ P'_{n'} \\ P'_{l'} \end{bmatrix} = \left\{ \begin{bmatrix} D_{ss'} & 0 & -D_{sl'} \\ 0 & 1 & 0 \\ D_{sl'} & 0 & D_{ss'} \end{bmatrix} \vec{P}_b + \begin{bmatrix} 0 \\ P(\theta) \\ 0 \end{bmatrix} \right\} \frac{1}{1 + P_n A_y}$$

where $P(\theta)$ is the polarization function of the target, A_y is the vector analyzing power for the reaction and the D coefficients are spin transfer coefficients (often referred to as the Wolfenstein parameters). The precession in the MRS dipole takes place about the $\hat{s}''$ axis, the polarization at the focal plane after spin precession in the magnetic field of the dipole is

$$\vec{P}'' \simeq \begin{bmatrix} 1 & 0 & 0 \\ 0 & \cos\chi & \sin\chi \\ 0 & -\sin\chi & \cos\chi \end{bmatrix} \vec{P}'$$

where χ is the Thomas precession angle of the proton spin and is given by

$$\chi = \gamma(\mu - 1)\alpha$$

where γ is the Lorentz factor; μ is the proton magnetic moment and α is the bend angle of the MRS ($60° \pm 3°$).

The measurements of the focal plane polarizations are explained in the next section. Here we assume they are known and see how to calculate Q in terms of these quantities.

$$P_{s''} = \frac{D_{ss'}P_s - D_{sl'}P_l}{1 + P_n A_y}$$

$$P_{n''} = \frac{D_{ss'}P_l - D_{sl'}}{1 + P_n A_y} \sin\chi + \frac{P_n + P}{1 + P_n A_y} \cos\chi$$

First we look at the case in which unpolarized incident beam was used. The solenoid polarities have no effect here. Thus we omit the label for polarities. By setting $\vec{P}_b = 0$, the above equations give

$$P^o_{s''} = 0 \qquad P^o_{n''} = P^o \cos\chi$$

or

$$P^o_{s''} = 0 \qquad P^o = \frac{P^o_{n''}}{\cos\chi}$$

where P^o is the induced polarization when using unpolarized beam(label o). In the data analysis two independent measurements of $P^o_{n''}(m), P^o_{n''}(p)$ have been used to calculate the P^o. The final result was obtained by averaging these two P^o values in order to get better statistics.

Measurement of $P_{s''}$ with various incident beam polarizations (spin up, $\uparrow$, and down, $\downarrow$, of the beam polarization before the solenoid positive, p, and negative, m, solenoid polarities) determine $D_{ss'}$.

$$P_{s''}(m\uparrow) = \frac{D_{ss'}P_s - D_{sl'}P_l}{1 + P_n A_y} \qquad P_{s''}(p\uparrow) = \frac{-D_{ss'}P_s - D_{sl'}P_l}{1 - P_n A_y}$$

$$P_{s''}(m\downarrow) = \frac{-D_{ss'}P_s + D_{sl'}P_l}{1 - P_n A_y} \qquad P_{s''}(p\downarrow) = \frac{D_{ss'}P_s + D_{sl'}P_l}{1 + P_n A_y}$$

Solving these equations gives

$$D_{ss'} = \left\{ P_s \left[\frac{1}{P_{s''}(m\uparrow) + P_{s''}(p\downarrow)} - \frac{1}{P_{s''}(m\downarrow) + P_{s''}(P\uparrow)} \right] \right\}^{-1}$$

Similarly from measuring $P_{n''}$ in the four polarized running modes we can determine $D_{sl'}, A_y$ and P. Since $|P_n| << 1$, the denominator $1/(1 + P_n A_y)$ can be expanded as $(1 - P_n A_y)$, then

$$P_{n''}(m\uparrow) = (P_n + A_y - P_n A_y^2)\cos\chi + \frac{D_{sl'}P_s + D_{ss'}P_l}{1 + P_n A_y}\sin\chi$$

$$P_{n''}(m\downarrow) = (-P_n + A_y + P_n A_y^2)\cos\chi + \frac{-D_{sl'}P_s - D_{ss'}P_l}{1 - P_n A_y}\sin\chi$$

$$P_{n''}(p\uparrow) = (-P_n + A_y + P_n A_y^2)\cos\chi + \frac{-D_{sl'}P_s + D_{ss'}P_l}{1 - P_n A_y}\sin\chi$$

$$P_{n''}(p\downarrow) = (P_n + A_y - P_n A_y^2)\cos\chi + \frac{D_{sl'}P_s - D_{ss'}P_l}{1 + P_n A_y}\sin\chi$$

Adding all four equations gives A_y

$$A_y = \frac{\sum_{ij} P_{n''}(i,j)}{4\cos\chi}$$

where $i = \{m, p\}$ and $j = \{\uparrow, \downarrow\}$. Here I should point out that the A_y's are basically induced polarizations which one could obtain with unpolarized beam. Thus we obtain the first check relation:

$$P^o = A_y$$

Other linear combinations give the longitudinal component of the beam polarization P_l, and $D_{sl'}$

$$P_l = \left\{ D_{ss'} \sin\chi \left[\frac{1}{P_{n''}(m\uparrow) - P_{n''}(p\downarrow)} - \frac{1}{P_{n''}(m\downarrow) - P_{n''}(p\uparrow)} \right] \right\}^{-1}$$

$$D_{sl'} = \frac{(1 + P_n A_y)(P_{n''}(m\uparrow) + P_{n''}(p\downarrow) - (1 - P_n A_y)(P_{n''}(m\downarrow) + P_{n''}(p\uparrow) - 4P_n\cos\chi}{4P_s \sin\chi}$$

It can be shown that the statistical errors for these quantities are [33]

$$\triangle D_{ss'} = \frac{1}{4P_s^2}\sqrt{P_s^2(\triangle A_s)^2 + A_s^2(\triangle P_s)^2}$$

$$\triangle D_{sl'} = \frac{1}{4\sin\chi P_s^2}\sqrt{P_s^2(\triangle A_n)^2 + A_n^2(\triangle P_s)^2}$$

$$\triangle P_l = \frac{1}{4\sin\chi D_{ss'}^2}\sqrt{D_{ss'}^2(\triangle A_n)^2 + A_l^2(\triangle D_{ss'})^2}$$

$$\triangle A_y = \frac{\triangle A_n}{4\cos\chi}$$

where

$$A_s = (P_{s''}(m\uparrow) + P_{s''}(p\downarrow)) - (P_{s''}(p\uparrow) + P_{s''}(m\downarrow)), \quad \triangle A_s = \sqrt{\sum_{ij}(\triangle P_{s''})^2}$$

$$A_n = (P_{n''}(m\uparrow) + P_{n''}(p\downarrow)) - (P_{n''}(p\uparrow) + P_{n''}(m\downarrow)), \quad \triangle A_n = \sqrt{\sum_{ij}(\triangle P_{n''})^2}$$

$$A_l = (P_{n''}(m\uparrow) + P_{n''}(p\uparrow)) - (P_{n''}(m\downarrow) + P_{n''}(p\downarrow)), \quad \triangle A_l = \triangle A_n$$

The longitudinal component of beam polarization should be always close to zero according to our assumption. From previouse experiment, we found that this component is very small.

4.4 Polarization of Scattered Protons

In this section, the method of measuring the polarization of scattered protons at the FPP is presented.

The azimuthal distribution of particles scattered in the focal plane polarimeter(FPP) is given by [28]

$$I(\phi_c, \theta_c) = I_0(\theta_c)(1 + \varepsilon_{n''}(\theta_c)\cos\phi_c + \varepsilon_{s''}(\theta_c)\sin\phi_c)A(\theta_c, \phi_c)$$

where $A(\theta_c, \phi_c)$ is the acceptance function of the the polarimeter ; θ_c and ϕ_c are the polar and azimuthal angles in the scattering from the carbon analyzer; $\varepsilon_{n''(s'')}$ is the asymmetry in the $\hat{n''}(\hat{s''})$ direction.

One requires that for a given θ_c all the azimithal angles ϕ_c must be possible in the acceptance function, i.e.

$$A(\theta_c, \phi_c) = A(\theta_c),$$

The condition imposed by this equation is checked by the "cone test". The detailed application of this condition is described in the vertex reconstruction section. Under this assumption and using the following the identity,

$$\int_0^{2\pi} F(\phi)\sin^m\phi\cos^n\phi d\phi = 0 \quad \text{if } F(\phi+\pi) = F(\phi),\ m+n = odd$$

and letting

$$\int_0^{2\pi} I(\theta_c, \phi_c)d\phi_c = N(\theta_c)$$

one can prove the following equations,

$$\int_0^{2\pi} I(\theta_c, \phi_c)\sin\phi_c d\phi = \frac{1}{2}N(\theta_c)\varepsilon_{s''}(\theta_c) \qquad \int_0^{2\pi} I(\theta_c, \phi_c)\cos\phi_c d\phi = \frac{1}{2}N(\theta_c)\varepsilon_{n''}(\theta_c)$$

Asymmetry and polarizations are related by:

$$\varepsilon_{n''}(\theta_c) = A_y(\theta_c)P_{n''} \qquad \varepsilon_{s''}(\theta_c) = -A_y(\theta_c)P_{s''}$$

where $A_y(\theta_c)$ is the analysing power of the carbon scatterer and $P_{n''}, P_{s''}$ are polarizations of the scattered particles at the focal plane after their precessions in the dipole. Then we may use the sum over all events for a probability integration, i.e. $\int_0^{2\pi} I(\theta_c, \phi_c) \rightarrow \sum_{ev}$,

$$\varepsilon_{n''}(\theta_i) = 2\frac{\sum_{ev} \cos\phi_c}{N(\theta_c)} = A_y(\theta_i)P_{n''}$$

$$\varepsilon_{s''}(\theta_i) = 2\frac{\sum_{ev} \sin\phi_c}{N(\theta_c)} = -A_y(\theta_i)P_{s''}$$

Where $\varepsilon_{n''(s'')}(\theta_i)$ is the asymmetry for the i'th θ_c bin in the $\hat{n}''(\hat{s}'')$ direction. All sums are evaluated for all events in the i'th bin. The statistical error in ε can be shown to be [28]

$$\delta^2(\varepsilon) = \frac{2}{N}(1 - \frac{\varepsilon^2}{2})$$

Putting the asymmetries from above into the distribution function, we get

$$I(\phi_c, \theta_c)A_y(\theta_c) = \frac{N(\theta_c)}{2\pi}[A_y(\theta_c) + A_y^2(\theta_c)P_{n''}\cos\phi_c - A_y^2(\theta_c)P_{s''}\sin\phi_c]$$

It is obvious that we apply the same technique as was used before to obtain,

$$\begin{aligned}\int_0^{2\pi} I(\theta_c, \phi_c)A_y(\theta_c)\cos\phi_c d\phi_c &= \int_0^{2\pi} \frac{N(\theta_c)}{2\pi}\cos^2\phi_c d\phi_c P_{n''}A_y^2(\theta_c) \\ &= \frac{1}{2}N(\theta_c)A_y^2(\theta_c)P_{n''} \\ &= [\frac{1}{2}\int_0^{2\pi} I(\theta_c, \phi_c)A_y^2(\theta_c)d\phi_c]P_{n''}\end{aligned}$$

or finally

$$P_{n''} = 2\frac{\int_0^{2\pi} I(\theta_c, \phi_c)A_y(\theta_c)\cos\phi_c d\phi_c}{\int_0^{2\pi} I(\theta_c, \phi_c)A_y^2(\theta_c)d\phi_c}$$

Substituting the event sum for the integrals, we have

$$P_{n''} = 2\frac{\sum_{ev} A_y(\theta_c)\cos\phi_c}{\sum_{ev} A_y^2(\theta_c)}$$

A similar equation holds for $P_{s''}$,

$$P_{s''} = -2\frac{\sum_{ev} A_y(\theta_c)\sin\phi_c}{\sum_{ev} A_y^2(\theta_c)}$$

The statistical error for P is given by [28]:

$$\delta^2(P_{n''}) = \delta^2(P_{s''}) = \frac{2}{\sum_{ev} A_y^2(\theta_c)}$$

During the event-by-event replay, the quantities $\sum_{ev} A_y(\theta_c)\cos\phi_c$, $\sum_{ev} A_y(\theta_c)\sin\phi_c$,$\sum_{ev} A_y^2(\theta_c)$ are accumulated and stored as focal plane coordinate spectra to allow extraction of transverse polarizations $P_{n''}$ and $P_{s''}$.

It should be noted that the proton energy loss in the carbon slabs need to be accurately evaluated, since A_y for carbon depends strongly on the proton energy below 200 MeV. Our carbon slabs have a surface density $\rho = 10.64 g/cm^2$. From the range plots, we calculate an energy loss of about 50 MeV. We assume the scatterings to taken place at the half thickness and an average energy of 175MeV. A_y values have been calculated from the empirical formula [32].

4.5 Data stream

For the online data taking, the MRS default event structure was used which accomodates variable length events with a fixed length part for TDC's and ADC's and a variable length part containing the TDC information from the MRS drift chambers. The drift chamber information from FEC and VDC's is in the form of wire numbers and drift times for the wires that were struck. All the IBP information is recorded by scalers periodically written onto tape without any condition checks. From these scalers the beam polarization was calculated on playback.

Data were analysed using the LISA computer code [29]. LISA is a general purpose and interactive data analysis program designed to process large amounts of event-mode data as they are commonly generated in nuclear physics experiments. The user can include special routines in the LISA eventloop (INSERT and EVBEV routines).

The data words for each event are the first checked by the drift routine. The function of this routine is to convert the TDC and ADC information to a position in each chamber. These positions are then tested whether they fall within predefined windows before storing them in an event buffer. Multiple hits are eliminated at this stage. The wire chamber positions are used in the INSERT routine to calculate focal plane coordinate, scattering angles, vertex position in the FPP and to perform the cone test. Focal plane and the FEC quantities are used to calculate the target quantities of interest (exitation energy, scattering angle, target projection) using a semi-empirical transformation matrix. This matrix is determined in first order by the MRS optics. Condition checks are applied to calculated quantities, events which pass through all condition checks are used to update five spectra which are necessary to evaluate the focal plane polarization:

$$CP = \sum_{ev} A_c(\theta)\cos\phi \qquad -\tfrac{\pi}{2} < \phi < \tfrac{\pi}{2}$$

$$CM = \sum_{ev} A_c(\theta)\cos\phi \qquad \tfrac{\pi}{2} < \phi < \tfrac{3\pi}{2}$$

$$SP = \sum_{ev} A_c(\theta)\sin\phi \qquad 0 < \phi < \pi$$

$$SM = \sum_{ev} A_c(\theta)\sin\phi \qquad \pi < \phi < 2\pi$$

$$AY = \sum_{ev} A_c^2(\theta)$$

From the formula derived in the previous section, we obtain:

$$P_{s''} = -2\frac{(CP - CM)}{AY}$$

$$P_{n''} = 2\frac{(SP - SM)}{AY}$$

The spectra (CP, CM, SP, SM) are binned in focal plane position to select the elastic events, and are also used to derive statistical errors.

Several cuts were applied to our data analysis. We only discuss the most important ones, the MRS acceptance and the proton identification. The MRS acceptance is determined essentially by the front end chamber which is mounted close to the target

chamber. Two gates together determine the overall MRS acceptance (X_o, Y_o). For a dispersed beam tune giving a narrow vertical beam illumination on target, the total acceptance of the spectrometer is determined by software cuts placed on $X_o$and Y_o, the FEC coordinates, so that data are accepted only in that range of θ and φ (which define the solid angle subtended by the FEC) over which the spectrometer acceptance is flat. The acceptance of the spectrometer is then computed as the solid angle of a simple square aperture. Typical solid angles are about 2.5 msr at large angles ($> 16°$) and about 0.75 msr at small angles ($< 16°$). The distance from the target to the middle of FEC was 64 cm at large angle and 133 cm at small angles.

The principle of charged particle identification is to measure the time of flight from the FEC to the focal plane(TTB) (linearly related to particle mass) and it's differential energy loss (ESUM) in any one of the trigger paddles (related to the square of particle charge). The pulse height in the trigger scintillator is proportional to the energy loss of the proton in the scintillator. Thus particles with similar mass but different charge or of the same charge but different mass will be separated in a two dimensional plot of TTB versus ESUM. This gives a clean separation of particle types.

Finally we need to mention the MRS resolution though it was not crucial to our measurement of spin observables. The optimum resolution of the MRS in dispersion matching mode is typically 100 keV at large angles and 140 keV at small angles. The difference in resolution is due mainly to multiple scattering in the wire chamber windows and is not dependent on energy. The resolution for this experiment was typically 270 KeV.

4.6 Vertex Reconstruction in the Focal Plane Polarimeter

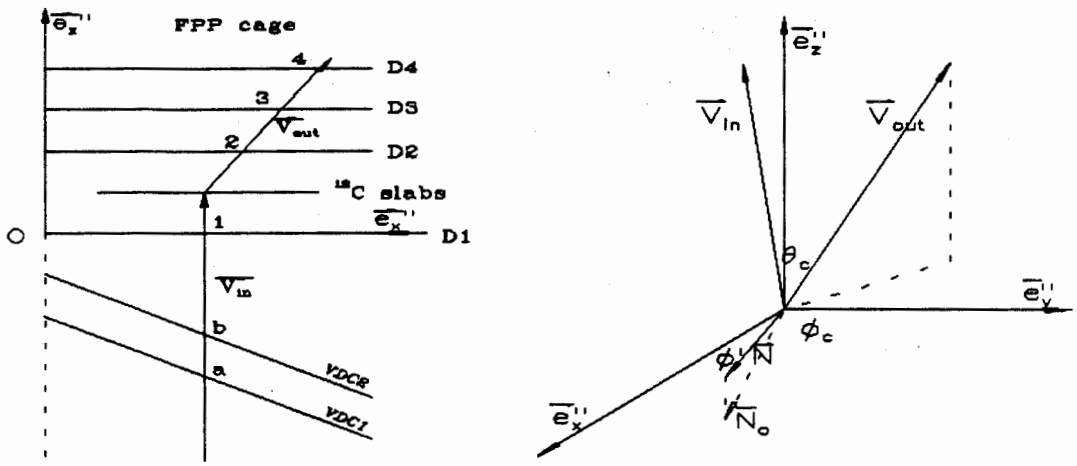

Figure 4.1: Vertex reconstruction in the FPP. Left is the FPP cage side view, right is the vector relation diagram

The FPP cage and relevant quantities are shown schematically in Fig 4.1. The drift decoding routine gives the positions of the particles in all wire chambers, we can use this information to obtain the scattering angle and azimuthal angle at the FPP and thus determine the angular distribution of the scattered protons at the carbon analyser. The focal plane polarization components can be extracted from this distribution according to the formulas given in the first section of this chapter. The following calculations are carried out in the focal plane frame.

The incoming particle trajectory toward the carbon slabs is determined by two sets of position coordinates measured by VDC1 and D1 which is just below the carbon analyser. The coordinates form an incoming vector (we choose normalized unit vector, so that the components of this vector are just the direction cosine to each axis.)

$$\vec{V}_{in} = (x_1 - x_a, y_1 - y_a, z_1 - z_a)/R_1$$

where $R_1 = \sqrt{(x_1 - x_a)^2 + (y_1 - y_a)^2 + (z_1 - z_a)^2}$, $(x_i, i = 1,2,3,4)$ are the position coordinates measured by the corresponding D chambers and (x_a, y_a, z_a) are the position measured by VDC1 (also in the focal plane frame). $\vec{V}_{in}$ can simply be written as

$$\vec{V}_{in} = (\alpha, \beta, \gamma)$$

where α, β, γ are direction cosines of $\vec{V}_{in}$.

Similarly, we construct the outgoing vector using the position information measured by D2 and D4 chambers which are after the carbon scatterer.

$$\vec{V}_{out} = (x_4 - x_2, y_4 - y_2, z_4 - z_2)/R_2$$

where $R_2 = \sqrt{(x_4 - x_2)^2 + (y_4 - y_2)^2 + (z_4 - z_2)^2}$.

$$\vec{V}_{out} = (\alpha', \beta', \gamma')$$

Then the scattering angle can be represented by:

$$\cos\theta_c = \vec{V}_{in} \cdot \vec{V}_{out} = \alpha\alpha' + \beta\beta' + \gamma\gamma'$$

The azimuthal scattering angle is calculated in the following way. We construct an intermediate vector which is perpendicular to both $\vec{V}_{in}$ and $\vec{V}_{out}$.

$$\vec{N} = \vec{V}_{in} \times \vec{V}_{out} = (\beta\gamma' - \beta'\gamma, \gamma\alpha' - \gamma'\alpha, \alpha\beta' - \alpha'\beta)$$

Then we project this vector into the x,y plane to obtain a new vector $\vec{N}_o$

$$\vec{N}_o = (\beta\gamma' - \beta'\gamma, \gamma\alpha' - \gamma'\alpha, 0)$$

From the right side of the figure 4.1, we get

$$\cos\phi' = \frac{N_{ox}}{|\vec{N}_o|} \qquad \sin\phi' = \frac{N_{oy}}{|\vec{N}_o|}$$

Since the azimuthal scattering angle is related to ϕ' through

$$\phi_c = 90° + \phi'$$

Thus

$$\cos\phi_c = -\frac{N_{oy}}{|\vec{N}_o|} \qquad \sin\phi_c = \frac{N_{ox}}{|\vec{N}_o|}$$

The closest approach distance between $\vec{V}_{in}$ and $\vec{V}_{out}$ can also be calculated. We set up a spectrum (Z0) to display the distribution of the closest approach distance and set a narrow gate on it. The events with the approach distance greater than 6mm are believed to result from multiple scattering and were rejected. we believe the $\vec{V}_{in}$ and $\vec{V}_{out}$ do not come from single event in such case.

Finally the cone test (to ensure that the acceptance function is independent of azimuthal scattering angle ϕ_c) has been applied. We use the scattering angle and vertex point in the carbon to construct a cone, with its axis parallel to $\hat{e}''_z$. If any part of this cone is outside of the FPP wire chambers, the event is also rejected since it would produce a false asymmetry which is not from scattering, but from the lack of detection in the FPP.

4.7 Angle Calibration

Determination of the exact scattering angle in scattering experiment is important because of sharp angular variation in the spin observables. The front end chamber in the MRS defines the solid angle for the scattering process and determines the scattering angle θ. It is difficult to mount the FEC in a position such that the center of the FEC matches exactly the measured angle.

From a kinematics graph (see Fig 4.2), one finds that protons scattering from differ-

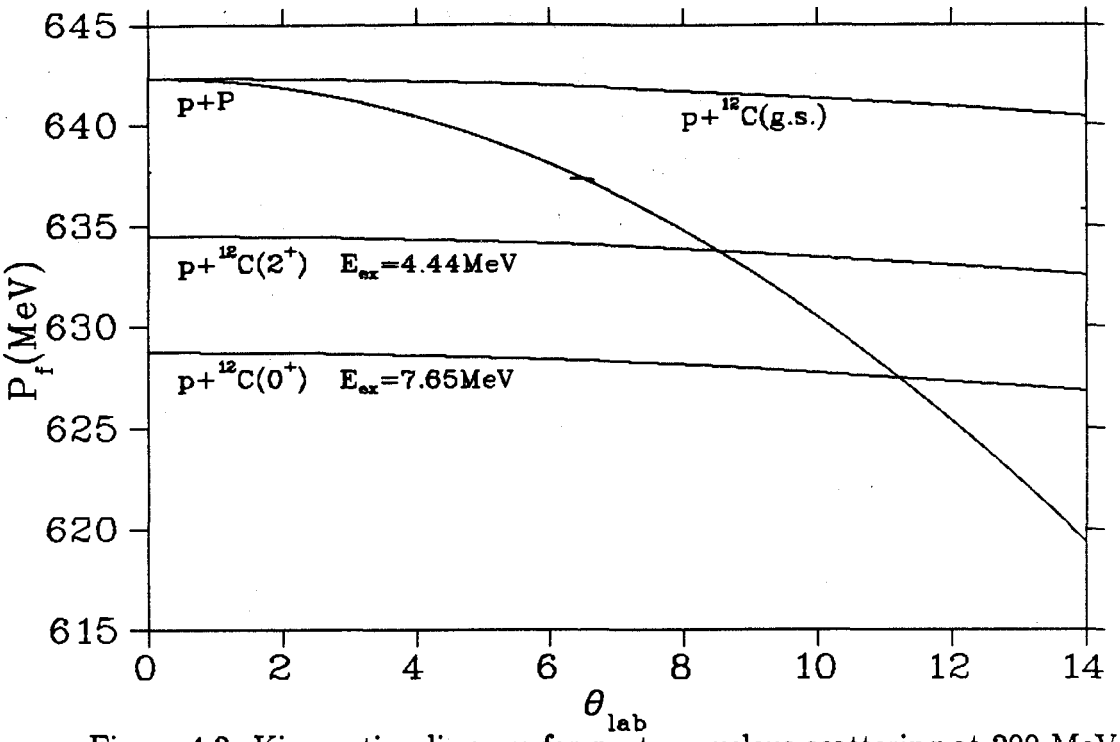

Figure 4.2: Kinematics diagram for proton-nucleus scattering at 200 MeV

ent targets have different outgoing momenta versus angle due to different target nucleus recoils. For light nuclei the momentum decreases rapidly with increasing scattering angle while for heavy nuclei the momenta of the scattered protons are nearly independent of angle. The kinematic curve for a heavy nucleus excited state will intercept that for a light nuclear groud state as shown in the figure. This crossing can serve as a calibration point. Since the crossing point is a purely kinematic effect determined by the mass of the target and the exitation energy of the target nucleus, it can be accurately calculated. In this experiment, data taken with a CH_2 target were used for the angle calibration. The crossing point for H ground state with the 4.44 MeV 2^+ state of ^{12}C was observed in a two-dimensional spectrum of Y_o versus X_F (see Fig. 4.3). Calculating the angle of the crossing point from the spectrum and comparing with the theoretical value, the scattering angle at the center of the FEC is determined. This angle offset will be taken

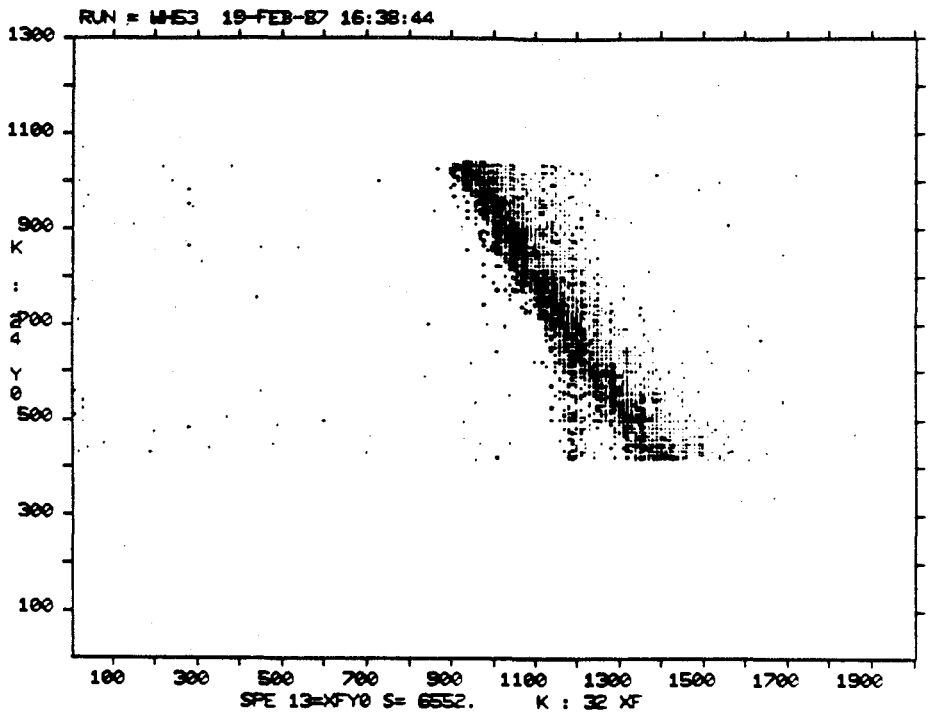

Figure 4.3: The focal plane spectrum at the crossing point.

into account in later analysis.

In large angle configuration, we have employed the kinematic crossing of H ground state and the 18 MeV 4^-, T=1 state in ^{16}O. For this purpose a "waterfall" target was used. Another method in which kinematic crossing between different states were forced by changing the magnetic field of the dipole proved unreliabe, probably because of differential effect in the magnet. We have determined the angle offset to be -0.17 ± 0.11 at small angles and -1.08 ± 0.10 for large angles.

Finally the polarization at the focal plane $P_{n''}$ and $P_{s''}$ were calculated from the areas of the elastic peaks in the 15 spectra (CM CP SM SP AY for spin up, down and off). Three pairs of these polarization components were subsequently fed into another program to calculate $P_l, D_{ss'}, D_{sl'}$ and Q using the formula provided earlier in this chapter.

Chapter 5

Results

In this chapter, we present our final results and conclusions. The first section contains a discussions of the reliability of the data and sources of error. The next section presents the comparison of the data with theories. The last section gives the conclusions drawn from this experiment.

5.1 Finite Bin-Size Effect

All physical detectors have a finite geometrical size which corresponds to a finite solid angle. The physical observables measured by these detectors are just weighted averages of their values at different angles. The weighting factor is the cross section since the detectors measure the number of particles. The distribution is determined by the properties of the spin observables. This detector size effect is pronounced when the observables fluctuate very rapidly with respect to the scattering angle and will attenuate the amplitude. This effect was first observed in the quadratic unitary check relation which is more sensitive then the spin observables to the finite bin-size effect. Thus

quadratic check holds only approximately.

$$\bar{D}^2_{ss'} + \bar{D}^2_{sl'} + \bar{P}^2 < 1.$$

In our experiment the angle bins were approximatly 1° wide. By calculating the weighted average of the theoretical predictions for the above quadratic relation, we find a similar structure that appears in our experimental data. (see Fig. 5.2). This suggests that the comparison between theory and experimental data is valid only after the same average is performed for the theoretical curves.

Suppose we have a spin observable O, then the average is defined by

$$\bar{O} = \frac{\int_{\theta_1}^{\theta_2} O(\theta)\sigma(\theta)d\theta}{\int_{\theta_1}^{\theta_2} \sigma(\theta)d\theta}$$

where θ_1 and θ_2 are the bin angle limits. The theoretical calculations shown in the following were all obtained with this procedure.

5.2 Consistency Checks and Systematic Errors

This experiment was run with the beam polarization in ten modes to perform a number of independent consistency checks. The basis for these checks was discussed in the previous chapter and the results are summarized here:

$$P_l \sim 0 \qquad P^o_{s''} = 0$$

$$P(\theta) = P^o(\theta)$$

$$D^2_{ss'} + D^2_{sl'} + P^2 = 1$$

where polarization $P(\theta)$ was derived from the measurements in the spin mode. while $P^o(\theta)$ was obtained from unpolarized measurements. Fig 5.3 and Fig 5.4 shows polarizations measured in spin-on and spin-off modes. The spin-on data have better statistics because of longer running times compared to the spin-off data. One notices good

agreement between these two sets of data. The agreement with previous A_y data from TRIUMF [9] is generally good although the latter exhibits slightly larger amplitudes at the large angles. The origin for these small discrepancies is not understood.

The quadratic consistency condition is very sensitive to false asymmetries present in the induced polarization and also to systematic errors.. The results of this check are displayed in Fig 5.2. The average deviation of the plotted quantily from unity is a direct measure of the net systematic error of the P. It should be noted that the largest deviations from unity occur exactly where the analyzing power is changing extremely rapidly. The cause of this deviation , besides the finite bin size effect, are not known. The measurement of the net value of the focal plane sideways polarization ($P^o_{s''}$) when using unpolarized beam also provides a way of checking the false sideways asymmetry in the FPP. The average value of $P^o_{s''}$ in ^{208}Pb measurement is 0.0068 ± 0.0082 and 0.011 ± 0.0084 in ^{90}Zr measurement (Fig. 5.1).

One source of systematic error in extracting the spin rotation parameter arises from the uncertainty in the determination of the beam polarization. Another possible source of systematic error is uncertainty in the analyzing power of the FPP analyzer. This analyzing power function was taken in an empirical form from reference [32]. Most of the systematic errors were canceled by reversing the spin of the incident beam. As we showed in the previous chapter, the inherent asymmetries of the beam polarization can be corrected in off line analysis. The average beam polarization for spin up incident beam is 0.778 and 0.793 for spin down incident beam.

5.3 Data and Theory

The general features of spin observables are their oscillatory behaviour. This behaviour arises from the diffraction phenomenon (Fraunhofer diffraction). The ^{90}Zr curves show fewer oscillations than ^{208}Pb , since its size is smaller than that of ^{208}Pb . The oscillation in polarization is related to the cross sections for spin-up and spin-down which both oscillate strongly, but have different periods. This leads to relatively smooth angular distributions of the unpolarized differential cross section (the sum of these two quantities), and a strongly oscillating polarization (the normalized difference of these two quantities). In terms of the optical potential, the reason for this behavior is that the spin-orbit force is comparable to the central force. This means that a spin-up proton feels a potential of larger radial range than a spin-down proton. The difference of size gives rise to the shift in the corresponding diffraction patterns. The amplitude of these observables depends on the nuclear structure and the effective NN interactions. The following section explains some of the features of these spin observables. Relativistic and nonrelativistic predictions are also provided to compare with our data.

In Fig 5.5 and Fig 5.6, we display the MOMP prediction for the Wolfenstein parameters. There is always a small angle shift at large angles but the amplitude agree with the data. The $D_{ss'}$ starts from 1 at 0°, since there is almost no interaction between the projectile and the target nucleus. No spin associated transitions occur here, thus $D_{ss'} = 1$ and $D_{sl'} = 0$. The small-angle $D_{ss'}$ data confirm that the empirical analysing power used for the carbon analyser [32] is correct.

The angular dependence of the vector analysing power P and the spin rotation function Q are shown in Fig. 5.7 and Fig 5.8. These results together with TRIUMF cross section data at 200MeV [9] (see Fig. 5.14) completely specify the scattering matrix

for elastic scattering. The dashed curves were calculated nonrelativistically using Von Geramb's density-dependent interaction derived from the Paris NN t-matrix [10]. The solid curves represent relativistic calculations carried out by Horowitz and Murdock [7]. They use pseudovector πN coupling and include Pauli blcoking.

The main aim of this experiment is to investigate the Pauli blocking effect in the nucleon-nucleus interaction. Fig 5.9 and Fig 5.10 display the RIA calculations with (solid) or without (dashed) Pauli blocking together with our data. The agreement of the full calculation with experiment is impressive.

One notices that Pauli blocking is a very large effect which is crucial to obtain an agreement between experiment and theory at this energy. The RIA calculation without Pauli blocking is out of phase at large angles and misses the structure at small angles. It also misses a structure observed in the polarization at small angle ($\sim 1.fm^{-1}$, Fig 5.9 and Fig 5.10) for both nuclei. At the same angle, the prediction for Q has the opposite sign to our data. It should be pointed out that Pauli blocking in the present RIA only modifies the imaginary optical potential by at most 10% and leaves the real potential almost unchanged. It implies that the imaginary optical potential plays an important role in the relativistic model. We conclude that Pauli blocking is an important medium effect at 200 MeV

We also compare the present RIA calculation with the MOMP calculation, (see Fig. 5.7 and Fig 5.8). Both RIA and MOMP predictions are in phase with the experimental data. Amplitude discrepancies are within 20%. The RIA calculations for Q are close to the data while the MOMP calculations predict the polarization better. Both theory curves tend to go out of phase with data at very large angles. In ^{90}Zr , the RIA predictions agree well with our data. The MOMP shows a small angle shift in Q at large angles but not in polarization. The discrepancy may be due to inaccurately known

parameters of the neutron density. Calculations show spin observables to be sensitive to different neutron densities [3]. The MOMP slightly underestimates the data around $0.62fm^{-1}$. In ^{208}Pb, the RIA calculation almost misses one Q structure at about $1.0fm^{-1}$, while the MOMP gives the right values at this point. Both theories give good descriptions at other angles. We also show cross sections together with two theoretical curves, see Fig 5.14 and Fig 5.4. The ^{208}Pb cross section data were taken from [9]. No ^{90}Zr data are available, so only the two theoretical curves are presented. The RIA and MOMP have no major disagreements until very large angles. The RIA calculation gives more structure at about 35° than the data.

5.4 Relativistic Effect in Von Geramb's Model

It was discovered a long time ago that the non-relativistic potential could not reproduce the cross section and the spin observables at the same time. It was found empirically [31][3] that if the optical potential is reduced by 20% (i.e. use $0.8U_{opt}$), then the calculations do reproduce these observables (See Fig. 5.11, 5.12 and 5.13). Later, it was believed that this factor is E/M where E is the total reduced energy and M is the reduced mass. But why does the non-relativistic theory need this factor which previously has only been justified empirically? Here I give a simple derivation.

The non-relativistic Schrödinger equation is

$$(\nabla^2 + k^2)\psi(r) = 2mV_{opt}\psi(r)$$

where $k^2 = 2mT$, T is the total kinetic energy, m is the reduced mass, V_{opt} is the optical potential.

Now I use the Klein-Gordon equation as a starting point. In the c.o.m. frame,

(where the vector part of the optical potential vanishes.), the equation of motion reads:

$$[p^2 + m^2 - (E - V_{opt}(r))^2]\psi(r) = 0$$

where E is the total energy in the c.o.m., V_{opt} is the scalar part of the optical potential. After the expansion, this equation becomes

$$(p^2 + m^2 - E^2)\psi(r) = [-2EV_{opt}(r) + V_{opt}^2(r)]\psi(r)$$

Using the Einstein mass-energy relation $k^2 = E^2 - m^2$, we substitute the momentum by its operator and omit the $V_{opt}^2(r)$ term since $E >> V_{opt}$, then

$$\begin{aligned}(\nabla^2 + k^2)\psi(r) &= 2EV_{opt}\psi(r) \\ &= \frac{E}{m}(2mV_{opt}(r))\psi(r)\end{aligned}$$

Thus solving the Schrödinger equation with relativistic kinematics and $\frac{E}{m}$ factor is equivalent to solving the first-order Klein-Gordon equation which is the relativistic equation of motion.

5.5 Conclusions

We have performed Q and A_y measurements for both ^{208}Pb and ^{90}Zr at 200MeV. The predictions of the microscopic optical model derived from both relativistic (RIA) and non-relativistic (MOMP) theories have been compared to our data. Since non-relativistic theory depends on the correction factor introduced in the relativistic equation of motion, relativity is also a crucial factor in 'non-relativistic' calculations. Without this factor, the MOMP will fail to reproduce the reaction cross section and lead to polarizations which are out of phase and of too small amplitude at relatively small angles (Fig. 5.11, 5.12 and 5.13). Both models include medium modifications which turn out

to cause very large effects in the spin observables. Systematic theoretical studies of the energy and mass dependence of Q are now possible. However, our data alone cannot provide clear evidence of the importance of relativistic effects. More experimental data involving inelastic and quasielastic scattering may shed some light on this problem.

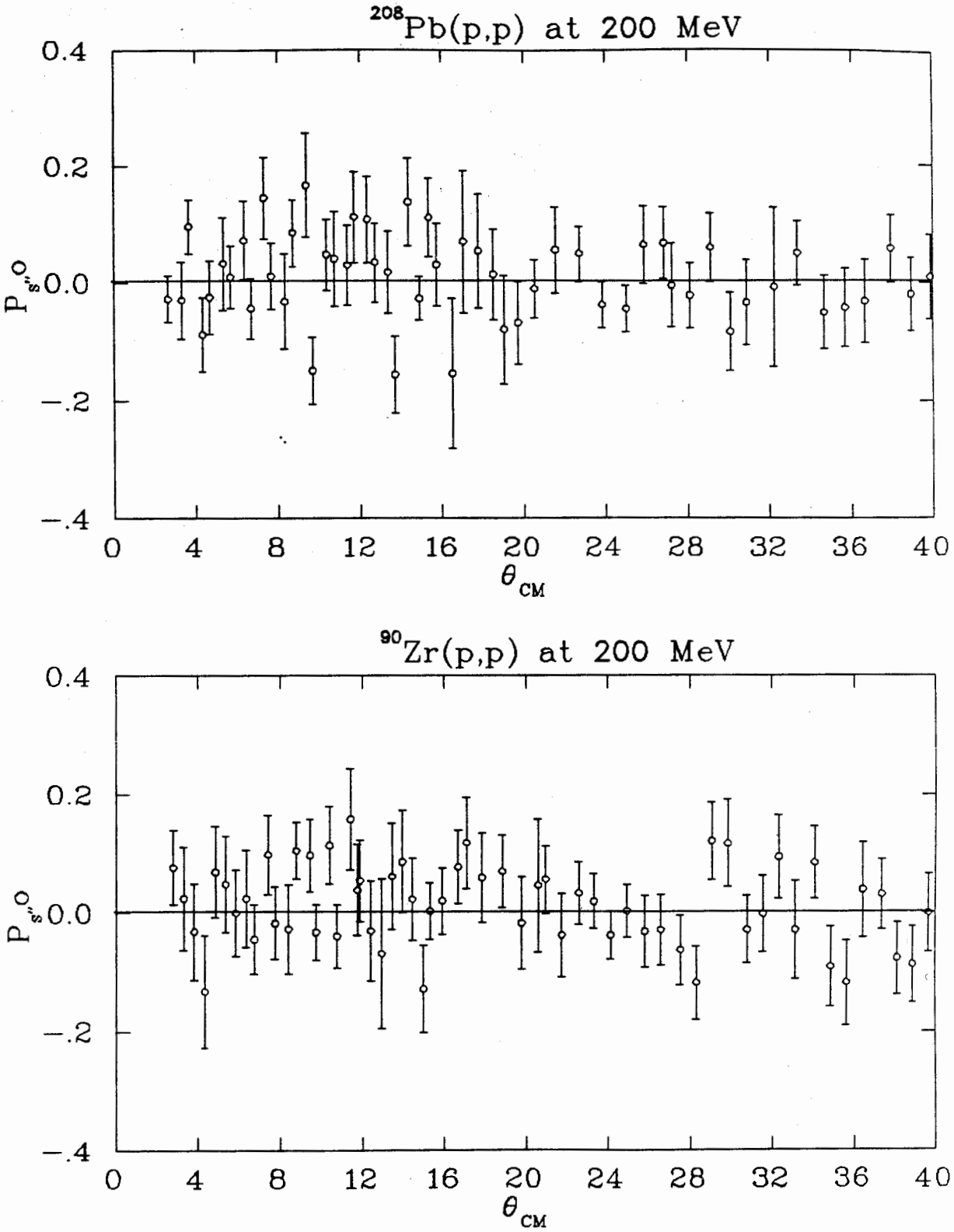

Figure 5.1: $P_{s''}$ when using unpolarized beam. Top is for ^{208}Pb and bottom is for ^{90}Zr

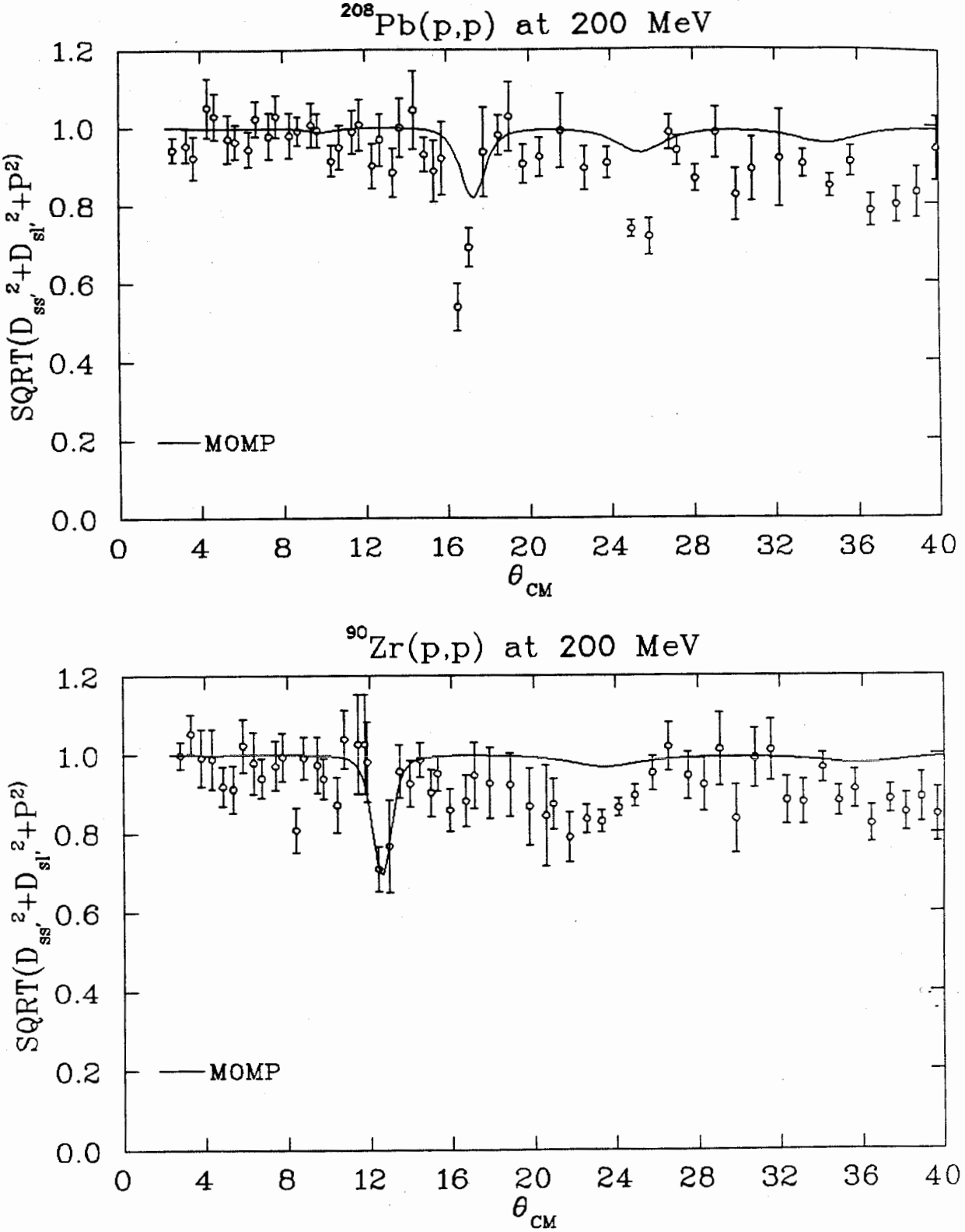

Figure 5.2: The quadratic unity check for ^{208}Pb (top) and ^{90}Zr (bottom). The solid curves are bined theoretical predictions from MOMP. Notice the similar structures between the data and the curves.

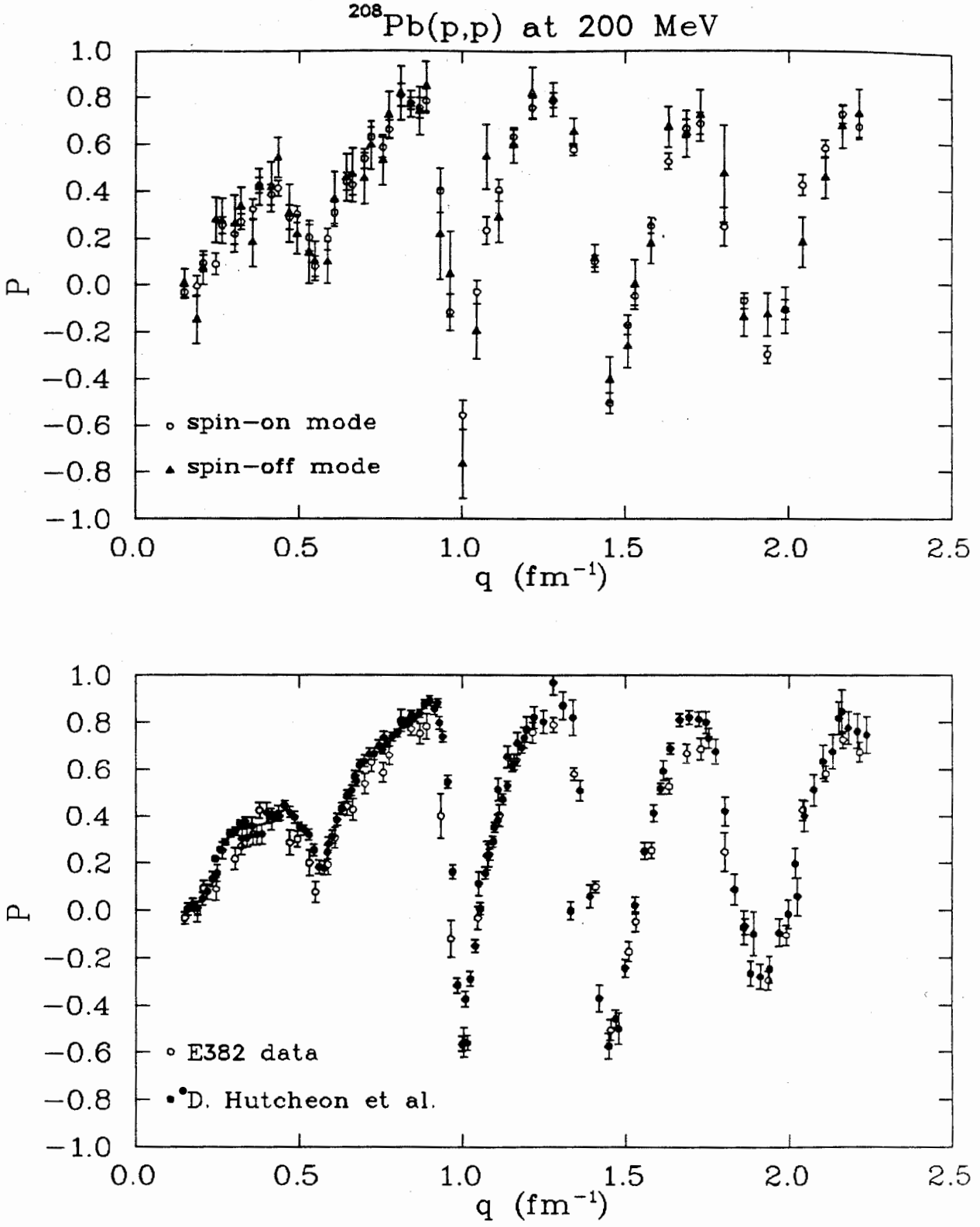

Figure 5.3: ^{208}Pb polarization plots (top), circular data points were taken with the spin mode crossed data points were taken with unpolarized incident beam. The comparison between TRIUMF A_y data and the P data from this experiment is shown at the bottom.

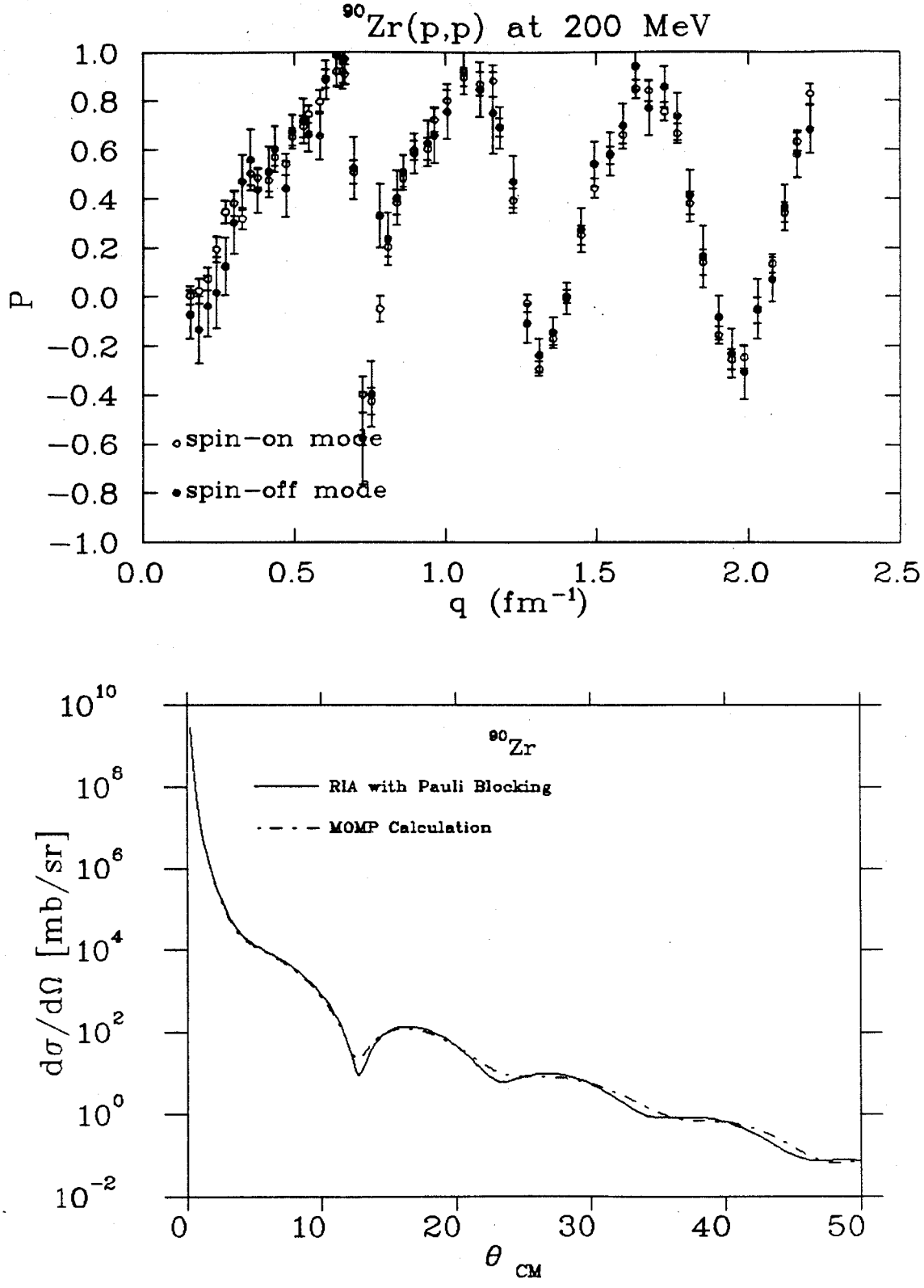

Figure 5.4: ^{90}Zr polarization plots (top), circular data points were taken with the spin mode crossed data points were taken with unpolarized incident beam. The comparison of cross sections calculated from RIA and MOMP is shown at the bottom.

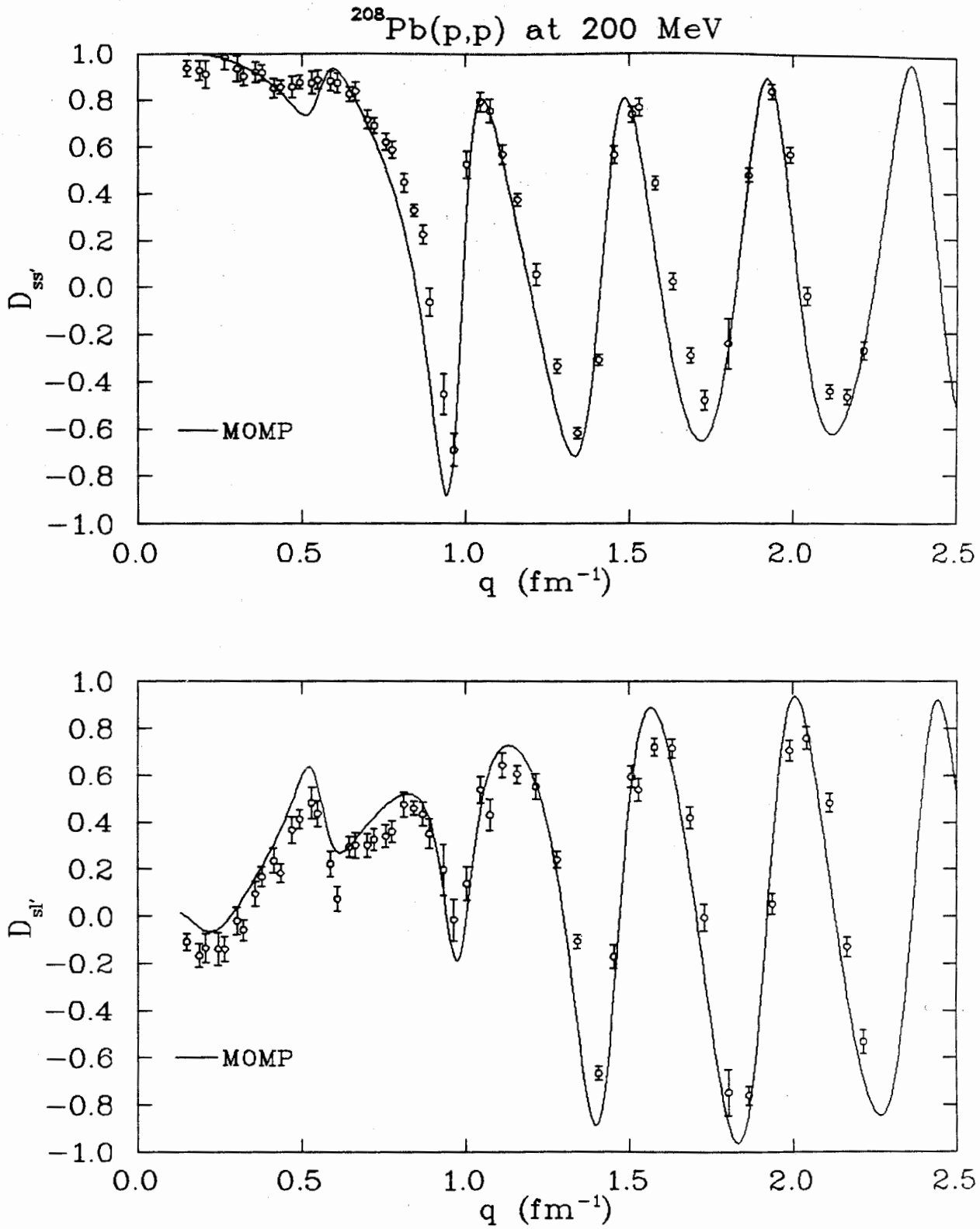

Figure 5.5: Wolfenstein parameters with MOMP predictions for proton scattering from ^{208}Pb.

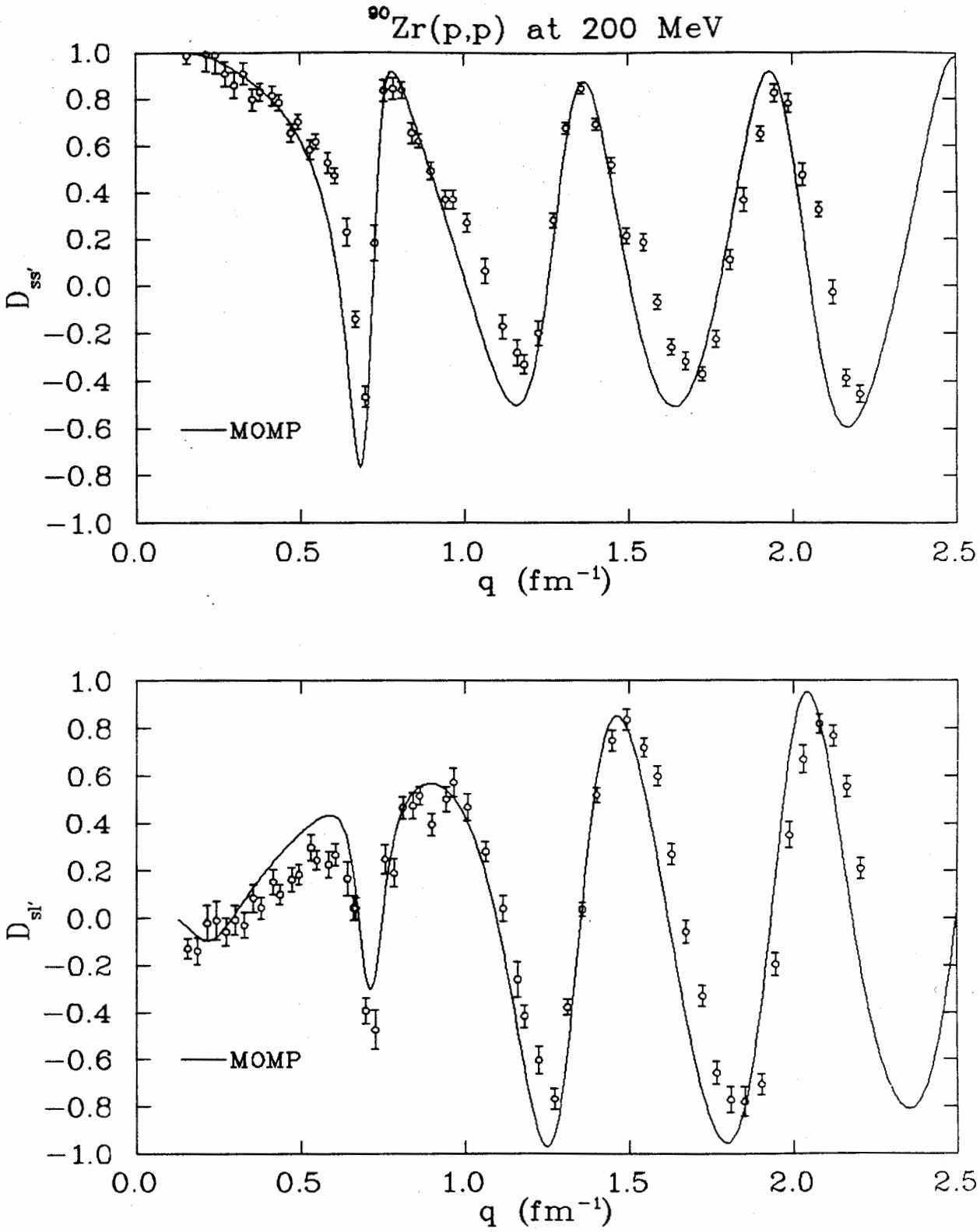

Figure 5.6: Wolfenstein parameters with MOMP predictions for proton scattering from ^{90}Zr .

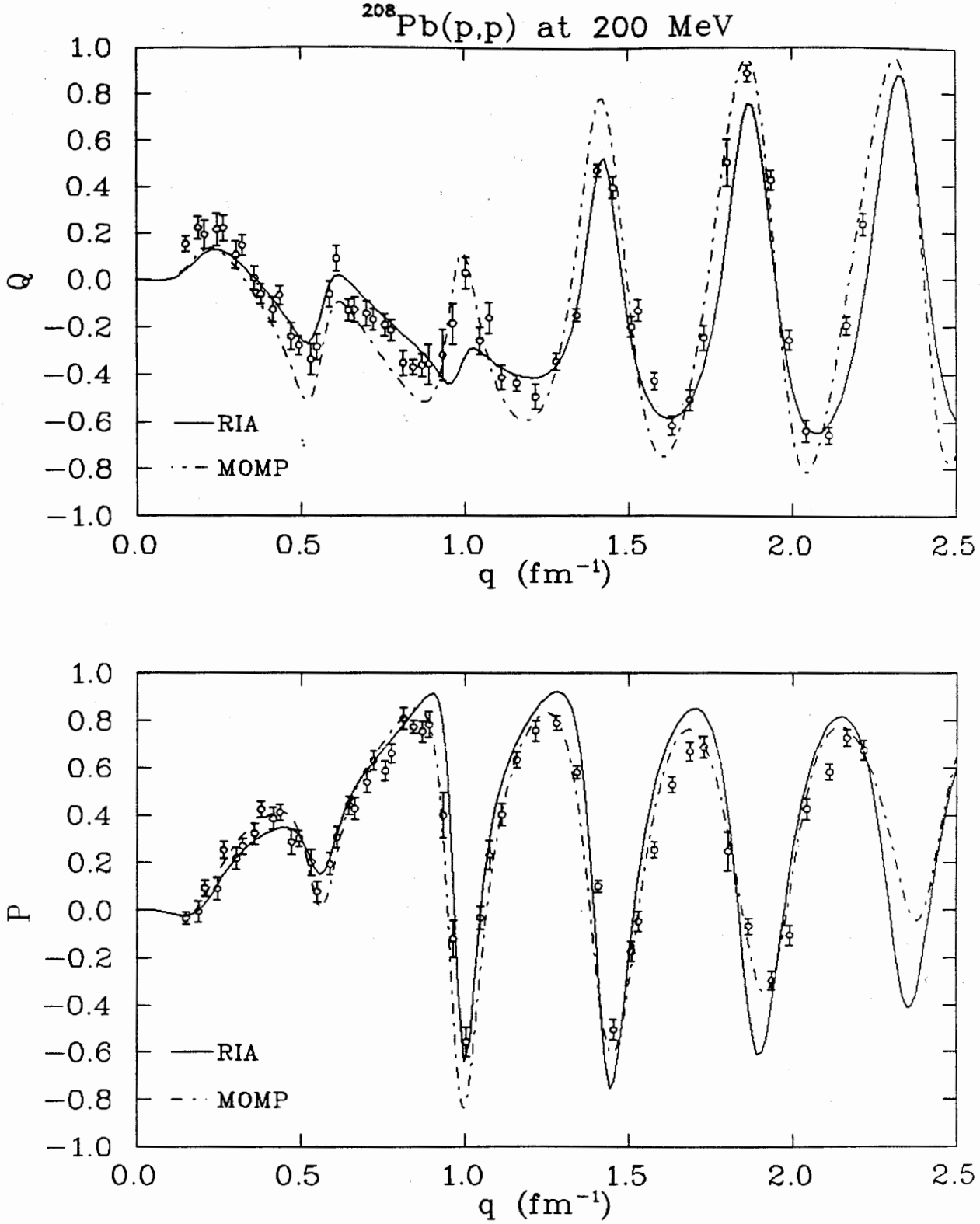

Figure 5.7: Spin rotation parameter Q and polarization P for ^{208}Pb (p,p). The solid curves correspond to the RIA including Pauli blocking and the dashed curve is the nonrelativistic density dependent calculations

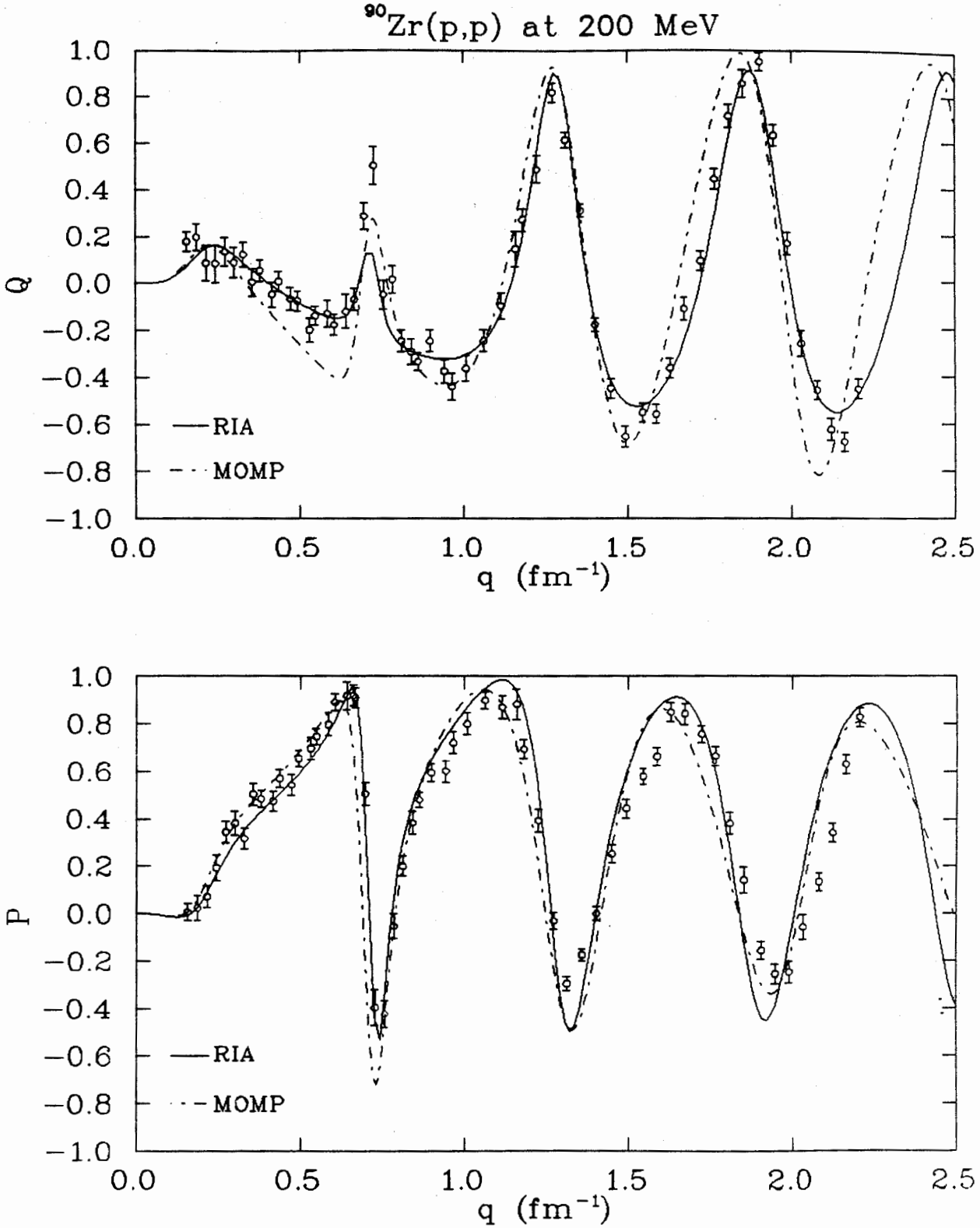

Figure 5.8: Spin rotation parameter Q and polarization P for ^{90}Zr (p,p). The solid curves correspond to the RIA including Pauli blocking and the dashed curve is the nonrelativistic density dependent calculations

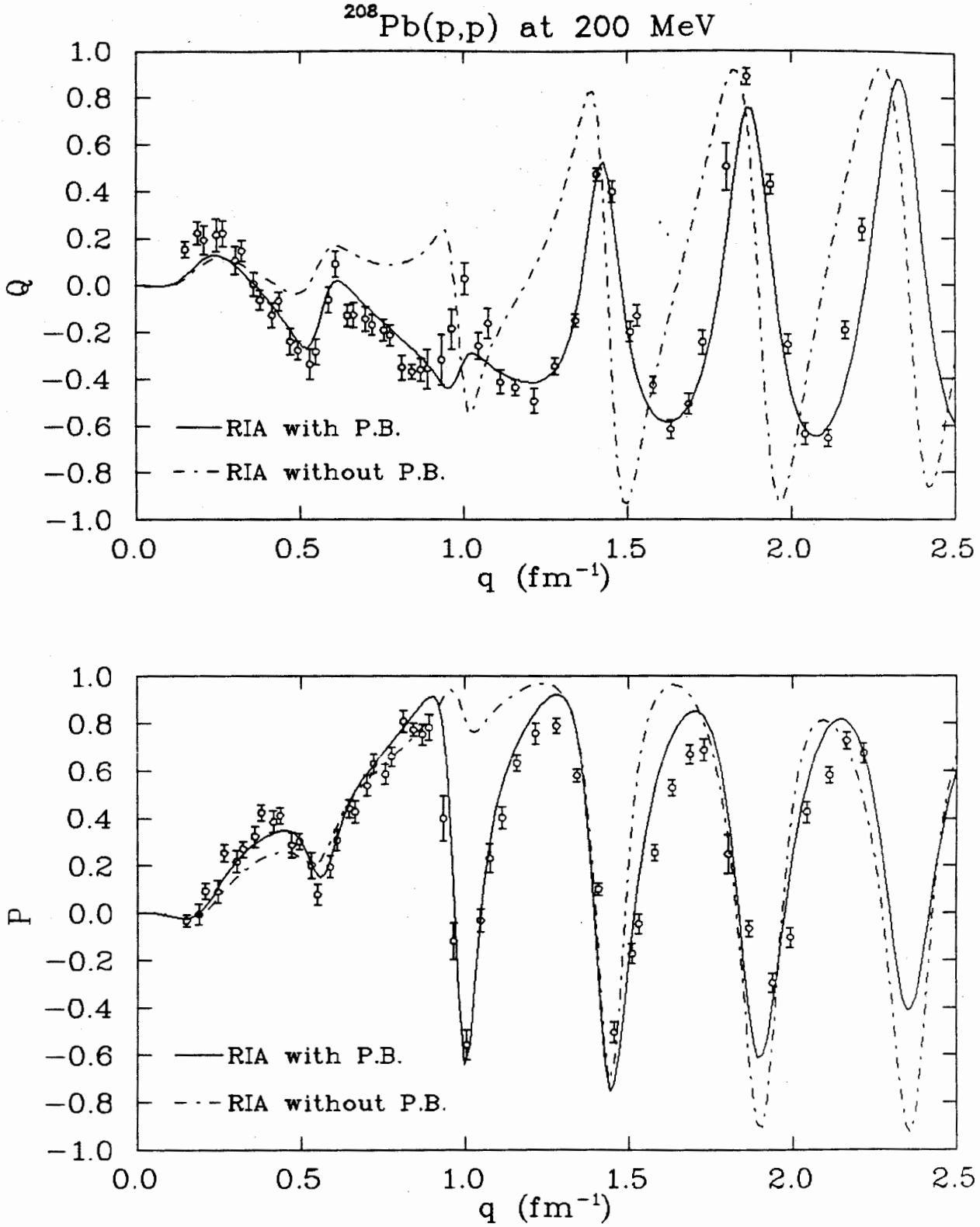

Figure 5.9: Spin rotation parameter Q and polarization P for ^{208}Pb (p,p). The solid curves correspond to the MRIA including Pauli blocking and the dashed curve is the same model without Pauli blocking

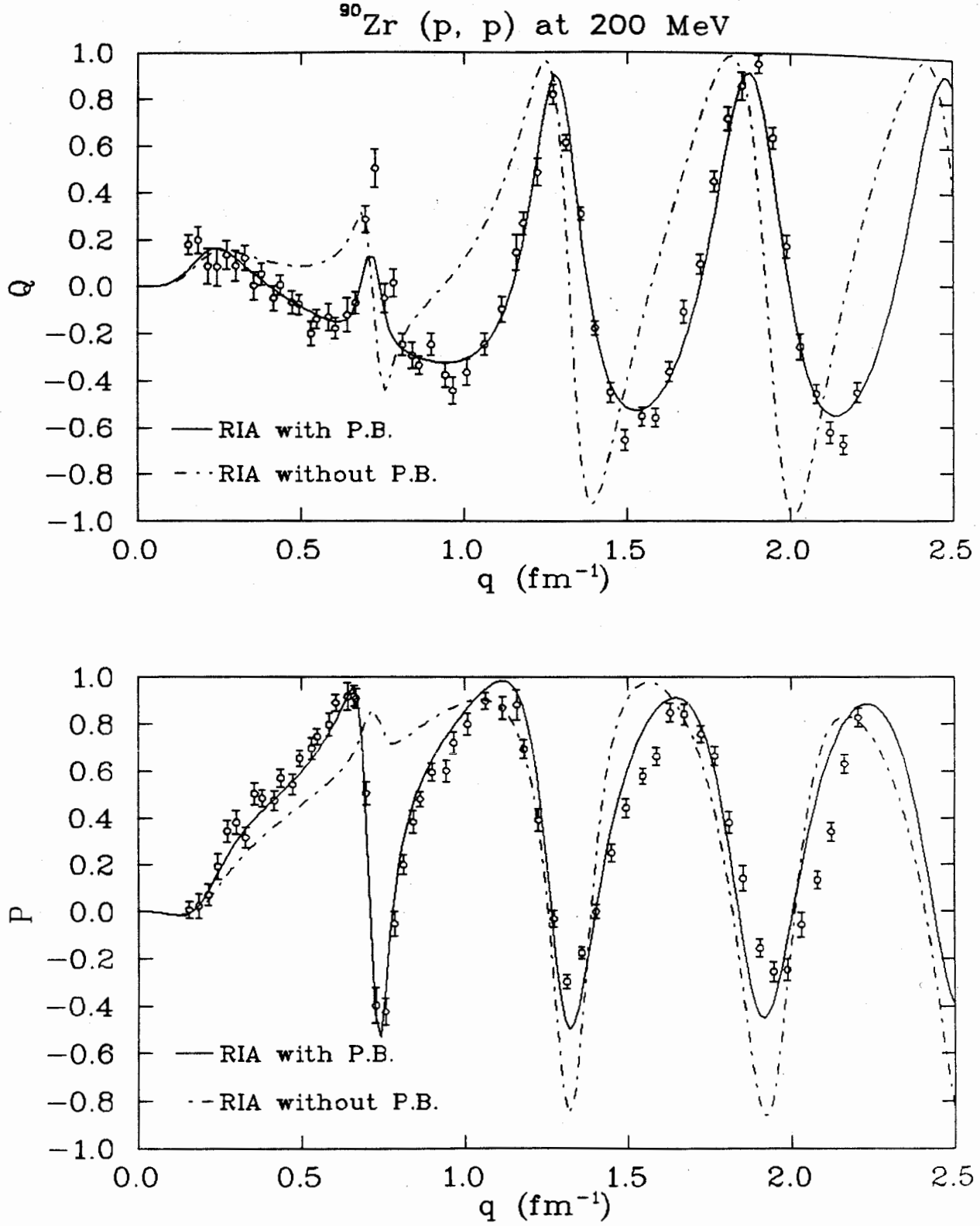

Figure 5.10: Spin rotation parameter Q and polarization P for ^{90}Zr (p,p). The solid curves correspond to the MRIA including Pauli blocking and the dashed curve is the same model without Pauli blocking

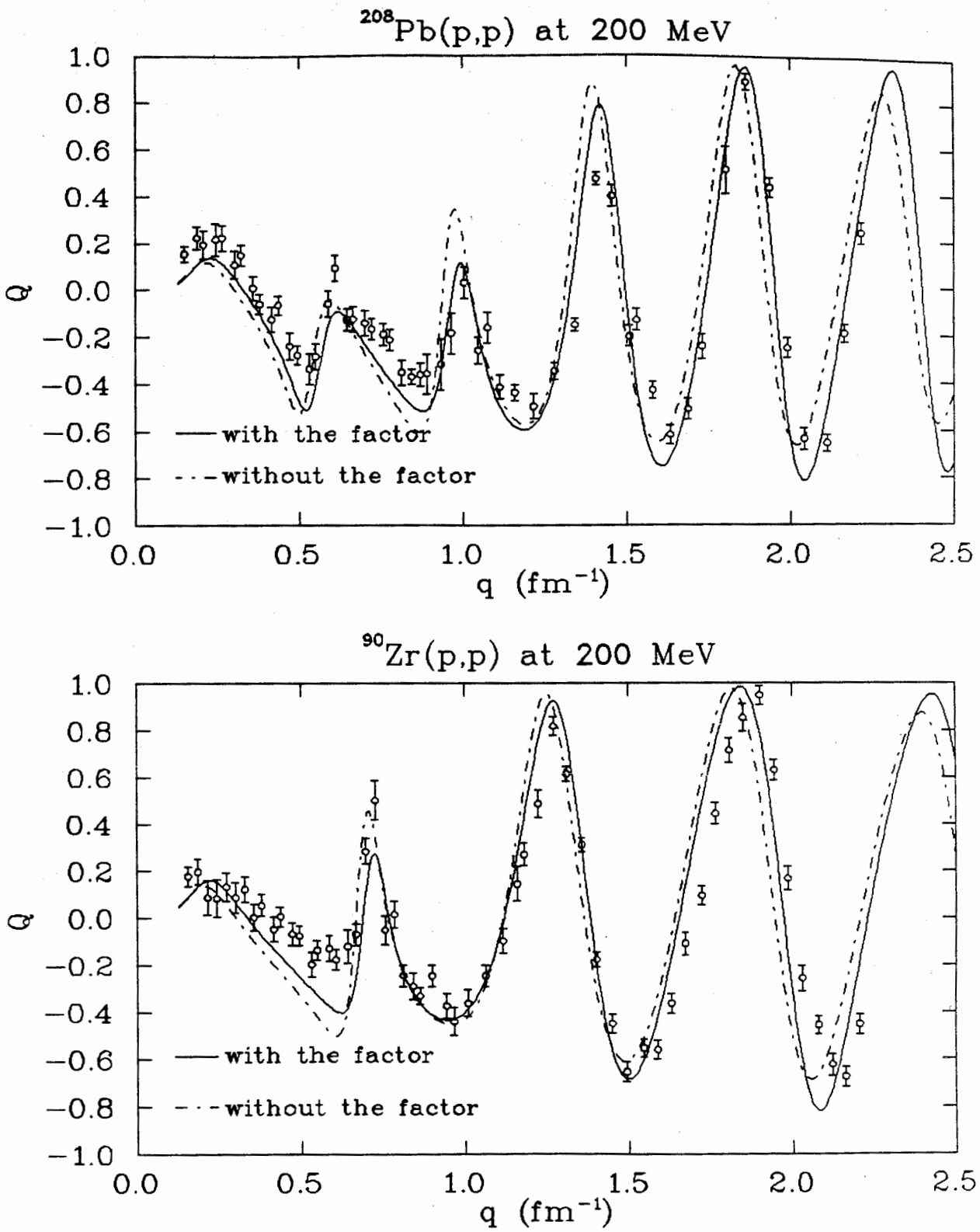

Figure 5.11: Q plots for MOMP calculations with and without the factor. Solid curves are calculated with the factor, the dashed curves are calculated without the factor.

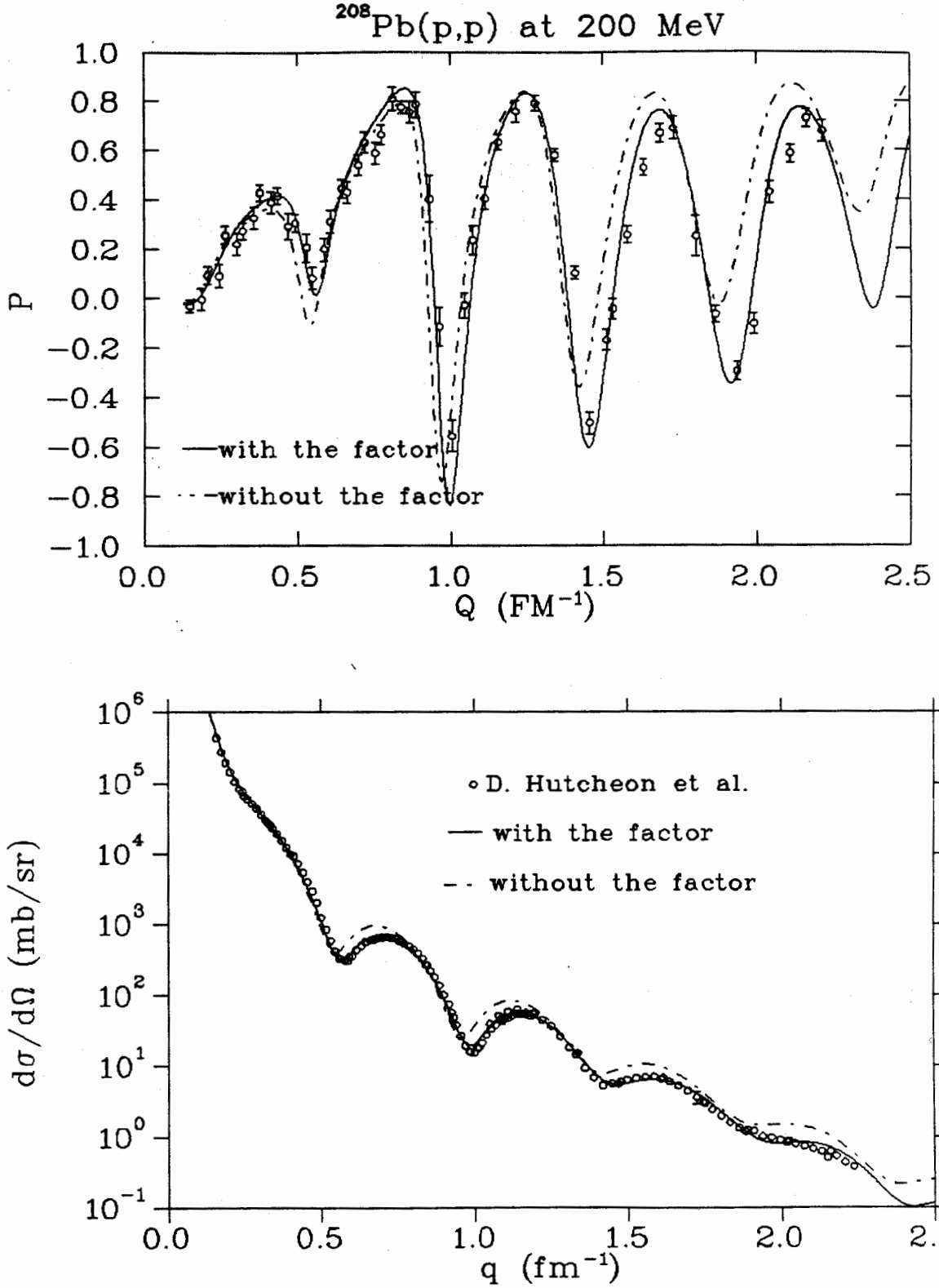

Figure 5.12: P and σ plots for ^{208}Pb from MOMP calculations with and without the factor. Solid curves are calculated with the factor, the dashed curves are calculated without the factor.

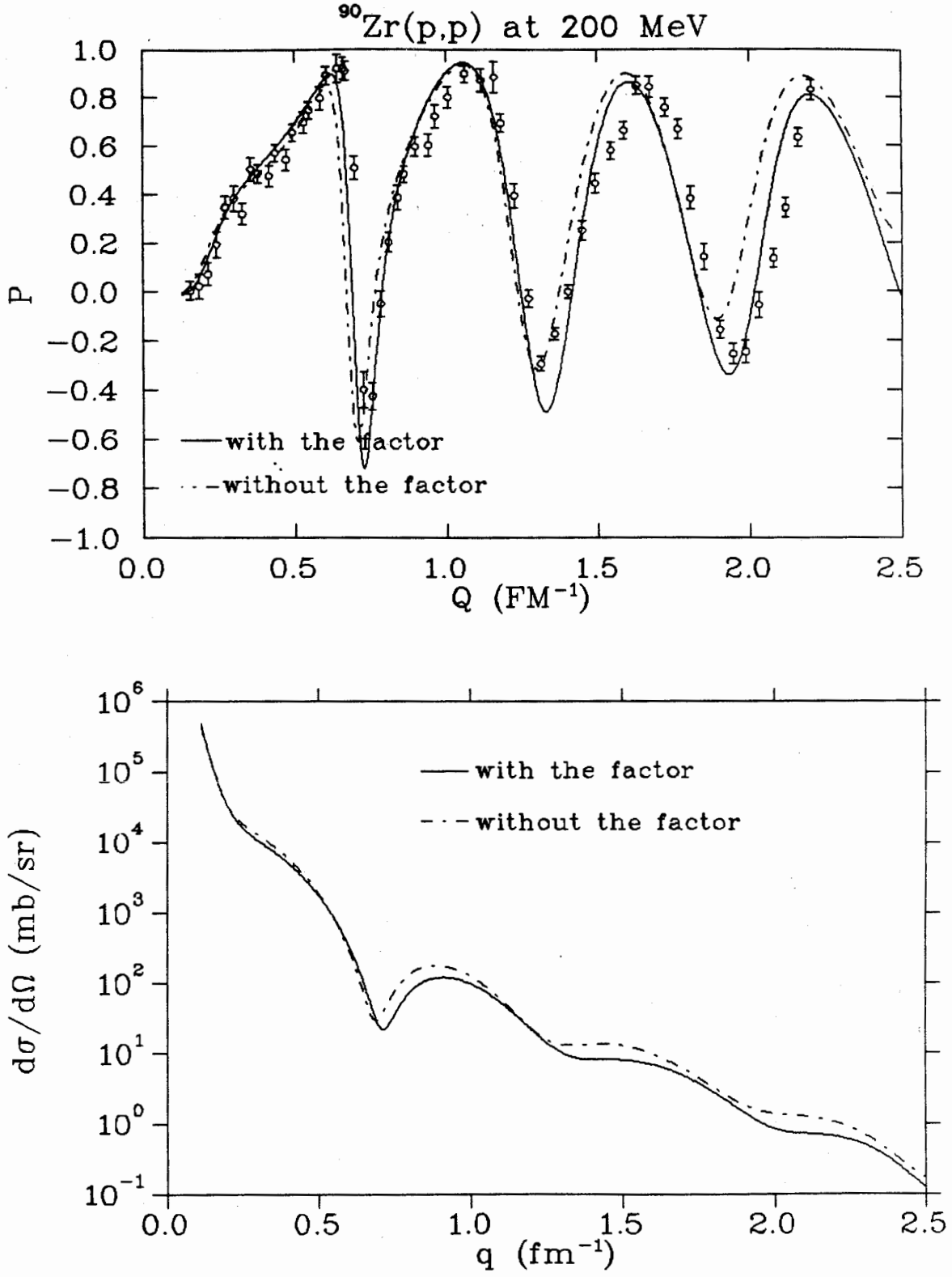

Figure 5.13: P and σ plots for ^{90}Zr from MOMP calculations with and without the factor. Solid curves are calculated with the factor, the dashed curves are calculated without the factor.

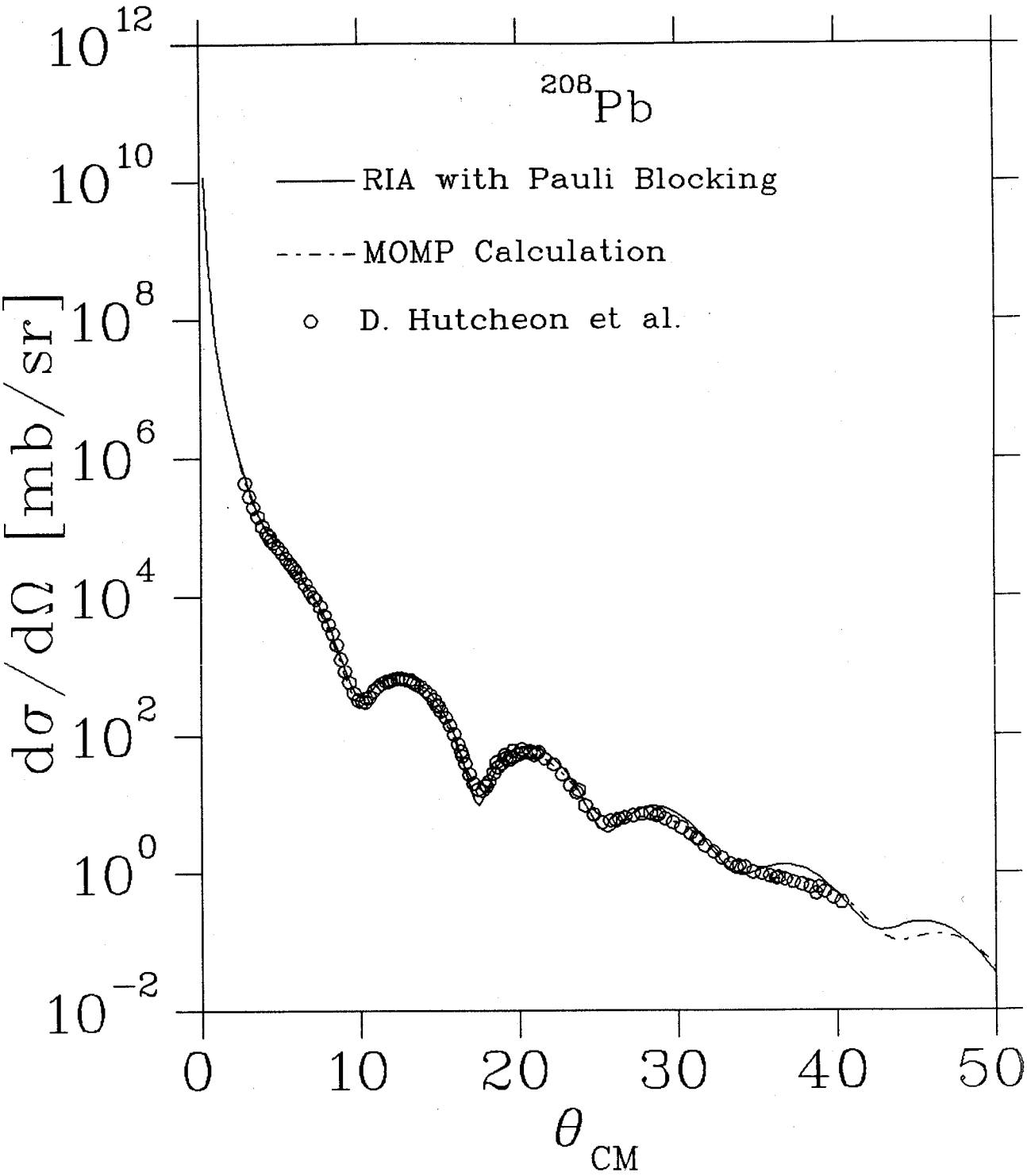

Figure 5.14: Cross section for 200 MeV proton scattering from ^{208}Pb . The solid curves represent calculations with RIA, the dashed curves are those with the MOMP.

200MeV Elastic Spin Observable Data for ^{208}Pb

θ_{cm}	Q	ΔQ	P	ΔP
2.630	0.152	0.035	-0.032	0.026
3.296	0.221	0.049	-0.005	0.043
3.655	0.193	0.062	0.093	0.035
4.321	0.215	0.069	0.090	0.047
4.675	0.220	0.054	0.254.	0.036
5.331	0.106	0.060	0.218	0.045
5.681	0.147	0.044	0.270	0.034
6.332	0.006	0.052	0.323	0.044
6.681	-0.061	0.041	0.424	0.034
7.332	-0.126	0.053	0.385	0.045
7.680	-0.066	0.039	0.412	0.034
8.324	-0.240	0.057	0.287	0.052
8.726	-0.276	0.041	0.302	0.035
9.386	-0.335	0.066	0.202	0.056
9.692	-0.283	0.053	0.079	0.044
10.387	-0.061	0.055	0.196	0.046
10.767	0.090	0.053	0.308	0.045
11.412	-0.128	0.045	0.442	0.038
11.743	-0.126	0.053	0.427	0.045
12.386	-0.143	0.051	0.538	0.043
12.747	-0.168	0.045	0.630	0.040
13.388	-0.190	0.047	0.586	0.043
13.729	-0.213	0.045	0.661	0.040
14.375	-0.351	0.052	0.808	0.047
14.908	-0.369	0.030	0.773	0.026
15.390	-0.361	0.049	0.754	0.044
15.762	-0.357	0.084	0.784	0.053
16.521	-0.318	0.107	0.400	0.094
17.068	-0.187	0.086	-0.118	0.078
17.793	0.027	0.069	-0.557	0.063
18.529	-0.260	0.055	-0.031	0.050
19.038	-0.164	0.064	0.233	0.059
19.732	-0.414	0.051	0.403	0.047
20.535	-0.438	0.035	0.633	0.032
20.535	-0.438	0.035	0.633	0.032
21.558	-0.496	0.052	0.758	0.044
22.708	-0.348	0.035	0.790	0.031
23.834	-0.151	0.029	0.580	0.026
25.003	0.473	0.028	0.101	0.025
25.860	0.400	0.047	-0.505	0.044
26.845	-0.199	0.044	-0.171	0.042
27.229	-0.130	0.046	-0.045	0.041

200MeV Elastic Spin Observable Data for ^{208}Pb (cont.)

θ_{cm}	Q	ΔQ	P	ΔP
28.126	-0.427	0.036	0.256	0.033
29.112	-0.615	0.039	0.528	0.034
30.089	-0.508	0.043	0.668	0.039
30.872	-0.242	0.052	0.687	0.046
32.222	0.506	0.101	0.250	0.082
33.355	0.888	0.037	-0.065	0.034
34.667	0.429	0.040	-0.295	0.039
35.671	-0.251	0.042	-0.103	0.042
36.642	-0.634	0.045	0.427	0.044
37.919	-0.652	0.036	0.583	0.035
38.917	-0.191	0.039	0.727	0.037
39.871	0.237	0.045	0.674	0.043

200MeV Elastic Spin Observable Data for ^{90}Zr

θ_{cm}	Q	ΔQ	P	ΔP
2.782	0.177	0.041	0.006	0.036
3.293	0.197	0.056	0.023	0.051
3.809	0.086	0.074	0.072	0.045
4.319	0.083	0.080	0.193	0.053
4.831	0.133	0.060	0.345	0.047
5.337	0.087	0.064	0.381	0.051
5.840	0.121	0.054	0.316	0.044
6.341	0.003	0.058	0.503	0.047
6.735	0.053	0.046	0.484	0.037
7.401	-0.049	0.052	0.474	0.043
7.749	0.006	0.042	0.570	0.037
8.407	-0.068	0.049	0.542	0.044
8.795	-0.076	0.042	0.654	0.035
9.456	-0.199	0.052	0.696	0.045
9.753	-0.138	0.041	0.746	0.035
10.409	-0.130	0.055	0.797	0.048
10.777	-0.177	0.045	0.891	0.037
11.434	-0.121	0.071	0.918	0.058
11.764	-1.334	77.347	0.919	0.045
11.900	-0.070	0.046	0.909	0.041
12.431	0.284	0.055	0.506	0.049
12.954	0.502	0.083	-0.398	0.074
13.463	-0.051	0.061	-0.425	0.055
13.965	0.015	0.058	-0.051	0.052

200MeV Elastic Spin Observable Data for ^{90}Zr (cont.)

θ_{cm}	Q	ΔQ	P	ΔP
14.463	-0.245	0.046	0.201	0.041
14.993	-0.291	0.055	0.383	0.049
15.314	-0.333	0.036	0.480	0.033
15.913	-0.246	0.045	0.595	0.039
16.691	-0.375	0.052	0.601	0.046
17.089	-0.440	0.058	0.720	0.047
17.855	-0.363	0.056	0.800	0.045
18.833	-0.246	0.045	0.898	0.036
19.794	-0.098	0.054	0.870	0.047
20.584	0.144	0.074	0.883	0.066
20.959	0.269	0.048	0.693	0.039
21.737	0.486	0.059	0.392	0.049
22.566	0.819	0.041	-0.030	0.036
23.302	0.614	0.033	-0.297	0.029
24.114	0.310	0.028	-0.175	0.026
24.927	-0.178	0.030	0.000	0.029
25.793	-0.450	0.041	0.251	0.038
26.577	-0.653	0.043	0.444	0.040
27.519	-0.552	0.039	0.579	0.035
28.281	-0.559	0.040	0.662	0.037
29.060	-0.363	0.043	0.848	0.039
29.845	-0.109	0.048	0.842	0.044
30.766	0.094	0.040	0.756	0.036
31.543	0.444	0.045	0.665	0.041
32.319	0.714	0.051	0.381	0.046
33.107	0.854	0.059	0.143	0.053
34.054	0.950	0.040	-0.155	0.037
34.832	0.630	0.045	-0.254	0.043
35.606	0.167	0.050	-0.246	0.047
36.402	-0.258	0.055	-0.055	0.053
37.320	-0.457	0.038	0.135	0.037
38.095	-0.622	0.046	0.342	0.039
38.868	-0.674	0.041	0.630	0.039
39.658	-0.452	0.042	0.828	0.041

Bibliography

[1] H. O. Meyer. *AIP conference Proceeding No. 97*

[2] J. Shepard et al, *Phys. Rev. Lett. 50 (1983) 1443*

[3] L. Rikus and Von Geramb *Nucl. Phys. A414 (1984) 413*

[4] O. Häusser et al, *Phys. Lett. B184 (1987) 316*

[5] A. Rahbar et al, *Phys. Rev. Lett. 47 (1981) 1811*

[6] R. W. Fergerson et al, *Phys. Rev. C33 (1986) 239*

[7] C. J. Horowitz and D. P. Murdock, *preprint, submited to Phys. Rev. C 1986*

[8] E. J. Stephenson *Antinucleon- and Nucleon Nucleus Interactions. edited by G. E. Walker et al, Plenum Press 1985*

[9] D. A. Hutcheon et al, *Phys. Rev. Lett. 47 (1981) 315*

[10] M. Lacombe et al, *Phys. Rev. C21 (1980) 861*

[11] J. Raynal *Preprint unpublished*

[12] C. W. De Jager et al, *Nucl. Data Tables 14 (1974) 479*

[13] L. Ray et al, *Phys. Rev. C18 (1978) 1756*

[14] F. A. Brieva and J. R. Rook *Nucl. Phys. A291 (1977) 299*

[15] C. J. Horowitz and B. D. Serot, *Nucl. Phys. A368 (1981) 503*

[16] C. J. Horowitz. *Phys. Rev. C31 (1985) 1340*

[17] W. N. Cottingham et al, *Phys. Rev. D8 (1973) 800*

[18] F. A. Brieva and J. R. Rook *Nucl. Phys. A297 (1978) 206*

[19] J. D. Bjorken and S. Drell *Relativistic Quantum Mechanics (McGraw Hill, New York) 1965*

[20] B. C. Clark et al, *The Interaction Between Medium Energy Nucleons in the Nucleus, edited by H. O. Meyer P. 260*

[21] K. Holinde et al *Nncl. Phys. A194 (1972) 161* 22

[22] Rudi Abegg *TRIUMF internal report*

[23] R. A. Arndt and D. Roper *VPI and SU Scattering Analysis Interactive Dial-In Program and Data Base*

[24] O. Häusser et al, *preprint*

[25] F. A. Brieva and J. R. Rook *Nucl. Phys. A291 (1978) 317*

[26] R. Henderson et al, *Nucl. Instr. and Meth. 254 (1987) 61*

[27] Gerald G. Ohlsen *Rep. Prog. Phys. 35 (1972) 717*

[28] J. B. McClelland *LAMPF report*

[29] D. Frekers *unpublished*

[30] C. J. Horowitz and M. J. Jqbal, *Phys. Rev. C33 (1986) 2059*

[31] R. Dymarz. *Phys. Lett. B152 (1985) 319*

[32] E. Aprile-Giboni et al, *Nucl. Instr. Meth. 215 (1983) 147*

[33] O. Häusser *E294 run plan*

[34] J. A. McNeil et al, *Phys. Rev. Lett. 50 (1983) 1439*

[35] G. W. Hoffmann et al, *Phys. Rev. Lett. 47 (1981) 1436*